



Estimating $ZZ \rightarrow ll\nu\nu$ background in the $ll + E_T^{miss}$ final state using $Z\gamma \rightarrow ll\gamma$ data

A Thesis

submitted to

Indian Institute of Science Education and Research, Pune
in partial fulfillment of the requirements for the
BS-MS Dual Degree Programme

by

Mangesh Sonawane

Registration Number: 20121083



Indian Institute of Science Education and Research, Pune
Dr. Homi Bhabha Road,
Pashan, Pune 411008, INDIA

June 2017 - April 2018

Conducted at : DESY
Notkestraße 85,
22607, Hamburg
Germany

Supervisor: Dr. Beate Heinemann
©Mangesh Sonawane 2018
All rights reserved

Certificate

This is to certify that this dissertation, entitled "Estimating $ZZ \rightarrow ll\nu\nu$ background in the $ll + E_T^{miss}$ final status using $Z\gamma \rightarrow ll\gamma$ data", submitted towards the partial fulfilment of the BS-MS dual degree programme at the Indian Institute of Science Education and Research (IISER), Pune, represents the work carried out by Mangesh Sonawane at the Deutsches Elektronen-Synchrotron (DESY), Hamburg, under the supervision of Dr. Beate Heinemann, Professor of Experimental Particle Physics at the Institute of Physics, University of Freiburg, during the academic year 2017-2018.

Mangesh Sonawane

Dr. Beate Heinemann

Committee:

Dr. Beate Heinemann

Dr. Seema Sharma

I dedicate this thesis to my parents, Avinash and Ranjana Sonawane, my mentors, Dr. Sourabh Dube and Dr. Seema Sharma, and to my friends and colleagues and IISER, without whose timely advice and support this thesis would not have been made possible.

Declaration

I hereby declare that the matter contained within the thesis entitled "Estimating $ZZ \rightarrow ll\nu\nu$ background in the $ll + E_T^{miss}$ final state using $Z\gamma \rightarrow ll\gamma$ data", contains the results of the work carried out by me at the Deutsches Elektronen-Synchrotron (DESY) Hamburg, under the supervision of Dr. Beate Heinemann, and the same has not been submitted elsewhere for any other degree.

Mangesh Sonawane

Dr. Beate Heinemann

Committee:

Dr. Beate Heinemann

Dr. Seema Sharma

Acknowledgements

I would like to express my deepest gratitude for Dr. Beate Heinemann for her guidance and patient mentoring. It's not just technical skills that I have acquired under her supervision, but also an understanding of how a physicist approaches the subject and tackles the inevitable problems that surface.

⟨ placeholder ⟩

Abstract

In the search for Dark Matter (DM) at the LHC, SM particles are produced in association with DM particles, which are invisible as they don't interact with the detector. Thus events with large imbalance in transverse momentum are of interest. One such signature is $ll + E_T^{miss}$. The dominant background contributing to the search for DM in the $ll + E_T^{miss}$ is $ZZ \rightarrow ll\nu\nu$. Currently, this background is determined using Monte Carlo simulation, with an uncertainty of $\approx 10\%$ [22]. The goal of this study is to establish a data driven method to estimate this background, and reduce the uncertainty. Using $Z\gamma \rightarrow ll\gamma$, which is a process with low backgrounds and has a high $BR \times \sigma$, it is possible to estimate the $ZZ \rightarrow ll\nu\nu$ contribution. In regions where $p_T(\gamma) \gg M_Z$, the two processes are kinematically similar. They have the same production mechanisms, but differ due to the photon and Z boson couplings to the quarks being different, as well as the difference in mass (photons are massless, while Z bosons are massive). Introducing a transfer factor R as the ratio $\sigma(ZZ)/\sigma(Z\gamma)$ which is determined from simulation, the contribution of $ZZ \rightarrow ll\nu\nu$ to the background can be estimated from $Z\gamma \rightarrow ll\gamma$ data. The uncertainty on the prediction of R due to theoretical aspects is estimated in this work.

Contents

| | |
|---|-----------|
| Abstract | i |
| 1 Introduction | 1 |
| 1.1 The Standard Model | 2 |
| 1.2 Inadequacies of the Standard Model | 4 |
| 1.2.1 Beyond the Standard Model | 4 |
| 1.2.2 Dark Matter | 5 |
| 2 The Large Hadron Collider | 9 |
| 2.1 History | 9 |
| 2.2 Design | 10 |
| 2.3 The ATLAS experiment | 11 |
| 3 Theoretical Aspects | 13 |
| 3.1 Invisible Higgs in association with a Z boson - ZH | 13 |
| 3.1.1 Selection Criteria | 13 |
| 3.1.2 Results of the ZH search | 14 |
| 3.2 Background estimation: ZZ | 15 |
| 3.3 Transfer factor R | 16 |
| 3.4 Theoretical Uncertainties | 16 |
| 3.5 Approach | 17 |
| 4 Transfer factor R and the uncertainties associated to it | 19 |
| 4.1 MCFM | 19 |
| 4.2 Preliminary Results | 20 |
| 4.2.1 Uncertainty from Missing Higher Order Corrections | 23 |
| 4.2.2 Uncertainty associated with Parton Distribution Functions | 26 |
| 4.2.3 Photon Fragmentation and Isolation Uncertainty | 27 |
| 5 Additional Figures | 29 |

Chapter 1

Introduction

Fundamental particle physics has a remarkable goal. It attempts to explain the interactions of matter and energy with the minimum possible number mathematical presumptions, with everything else in the universe being an emergent property.

Not only is it remarkably ambitious, the Standard Model of physics is one of the most successful theories developed, describing the fundamental particles and their interactions [1]. It is theoretically self-consistent, and has enjoyed tremendous success in providing accurate experimental predictions. However, the Standard Model is not complete theory of fundamental interactions. It does not provide an explanation for several observed phenomena, such as gravity, or the accelerating expansion of the universe, among others.

One such question that triggers burning curiosity is the apparent incongruity of galaxy rotation curves with the theory of Newtonian mechanics: stars in the arms of spiral galaxies appear to move much faster than Newtonian physics would predict. Either the current understanding of mechanics is incomplete, or there is more mass present somewhere in the galaxy that is not visible by any method that is currently employed. This invisible hunk of matter is what is termed as Dark Matter (DM).

Detailed observations of these rotation curves, along with measurements of other phenomena such as gravitational lensing by distant galaxies, galaxy clusters, and Cosmic Microwave Background (CMB) lead to the conclusion that, if the Dark Matter hypothesis is true, the amount of visible Baryonic matter in the universe is a mere 4%. The remaining 96% of the universe is composed of Dark Matter and Dark Energy.

Now it becomes important to address the question: what exactly is Dark Matter?

Several extensions to the Standard Model, called Beyond Standard Model (BSM) theories, attempt to provide an explanation of these observed phenomena. Dark Matter hasn't been observed to interact directly through the electromagnetic force, and are thus invisible to current detectors. Consequently candidates for Dark Matter are called Weakly Interacting Massive Particles (WIMPs). In LHC experiments, events with WIMPs in the final state show up as an imbalance in the momentum in the plane transverse to the beam (referred to as E_T^{miss} throughout this thesis).

One such BSM theory postulates that these Dark Matter candidate particles may couple to Standard Model particles in interactions mediated by the Higgs boson. Fig 1.1 illustrates some of the possible processes for the production of the Higgs boson. The Higgs boson can then decay into invisible particles.

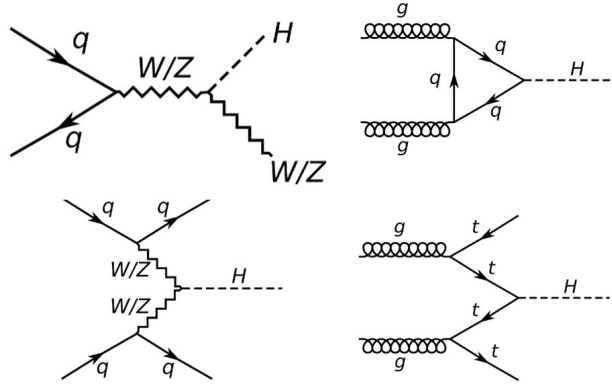


Figure 1.1: Feynman diagrams for the Standard Model production of the Higgs boson; VH: Higgs produced in association with a W/Z boson (top left), ggF: gluon-gluon fusion (top right), VBF: vector boson fusion (bottom left), ttH: (bottom right). The Higgs boson then further decays into invisible DM particles.

High energy collision experiments conducted at detectors are a method to experimentally investigate the predictions made by particle physics in a controlled manner. Several other kinds of detector experiments, both passive and active, investigate phenomena such as neutrino flavor oscillations and direct dark matter searches. The Large Hadron Collider (LHC), built and operated by CERN, is a proton-proton (and heavy ion) collider located in Switzerland and France, is the largest such collider in the world. It has provided invaluable data since commencing operations in 2008, providing experimental confirmation for phenomena such as the Higgs boson.

This chapter gives an overview of the Standard Model, it's constituent matter particles, forces, and their interactions. It also delves into the shortcomings of the Standard Model, and introduces some ways in which Dark Matter is probed at the LHC. Chapter 2 describes the LHC, as well the ATLAS detector.

In this thesis, a closer look is taken at the VH channel, in particular ZH, where the Higgs boson decays invisibly into DM particles, and the Z boson decays into a dilepton pair. The signature of such a process is $ll + E_T^{miss}$. A possible search in this channel would constitute stacking all known Standard Model processes that contribute to the $ll + E_T^{miss}$ signal (making up the background) and look for excesses in data which will indicate the presence of non-Standard-Model processes. In this thesis, a closer look is taken at the $ZZ \rightarrow ll\nu\nu$ process, which constitutes the dominant SM background in the $ll + E_T^{miss}$ final state. However, it is difficult to discriminate between the Standard Model $ZZ \rightarrow ll\nu\nu$ and $ZH \rightarrow l^+l^- + E_T^{miss}$, the process under consideration, because of the identical final state. Thus, an attempt is made to estimate it using alternate processes with clean signals.

Chapter 3 discusses the theoretical aspects of investigating the $ZZ \rightarrow ll\nu\nu$ contribution, and chapter 4 presents the results obtained during the course of this thesis.

1.1 The Standard Model

The Standard Model is the name given to the theory of particles, fundamental forces, and interactions that govern the Universe. It describes three of the four forces: the electromagnetic, strong and weak forces. Figure 1.2 shows a schematic representation of the elementary particles in the Standard Model.

The Standard Model classifies fundamental particles as either Fermions or Bosons:

- **Fermions:** make up the matter in the universe. Fermions are spin 1/2 particles, and are categorized into quarks and leptons. Quarks exist in 6 flavors, up, down, charmed, strange, top (or truth) and bottom (or beauty). Leptons too exist in 6 flavors: electrons, muons, and taus, and their respective neutrinos. The up, charmed and top quarks carry an electric charge of

$+2/3e$. The down, strange and bottom quarks carry an electric charge of $-1/3e$. The electron, muon and tau carry an electric charge of $-1e$, and the neutrinos carry no electromagnetic charge. Here, e is the unit of electromagnetic charge, and is equal to 1.602×10^{-19} Coulombs. Quarks and leptons are divided into three generations, with each generation having more mass than the last. Each fermion has a parity inverted counterpart, called an anti-particle, having the same mass, but an opposite charge. For example, an anti-electron (or a positron) has a charge of $+1e$ and a down anti-quark will have charge of $+1/3e$.

- **Bosons:** are particles with integral spin that mediate the interactions between particles in the universe. There are four gauge bosons: the photon, which mediates electromagnetic interactions, the W and Z bosons that mediate weak interactions, and the gluons, which mediate strong interactions. These are vector bosons, having spin $+1$. In addition, there is a scalar boson (spin 0), the Higgs boson, which gives particles their mass.

Standard Model of Elementary Particles

| three generations of matter (fermions) | | | | | |
|--|--|---|--|--|----------------------------------|
| | I | II | III | | |
| mass | $\approx 2.4 \text{ MeV}/c^2$ | $\approx 1.275 \text{ GeV}/c^2$ | $\approx 172.44 \text{ GeV}/c^2$ | 0 | $\approx 125.09 \text{ GeV}/c^2$ |
| charge | $2/3$ | $2/3$ | $2/3$ | 0 | 0 |
| spin | $1/2$ | $1/2$ | $1/2$ | 1 | 0 |
| QUARKS | u up | c charm | t top | g gluon | H Higgs |
| | $\approx 4.8 \text{ MeV}/c^2$ $-1/3$ $1/2$ d down | $\approx 95 \text{ MeV}/c^2$ $-1/3$ $1/2$ s strange | $\approx 4.18 \text{ GeV}/c^2$ $-1/3$ $1/2$ b bottom | 0 0 1 γ photon | |
| | $\approx 0.511 \text{ MeV}/c^2$ -1 $1/2$ e electron | $\approx 105.67 \text{ MeV}/c^2$ -1 $1/2$ μ muon | $\approx 1.7768 \text{ GeV}/c^2$ -1 $1/2$ τ tau | 0 1 Z Z boson | |
| LEPTONS | $< 2.2 \text{ eV}/c^2$ 0 $1/2$ ν_e electron neutrino | $< 1.7 \text{ MeV}/c^2$ 0 $1/2$ ν_μ muon neutrino | $< 15.5 \text{ MeV}/c^2$ 0 $1/2$ ν_τ tau neutrino | $\approx 80.39 \text{ GeV}/c^2$ ± 1 1 W W boson | |
| | | | | | GAUGE BOSONS |
| | | | | | SCALAR BOSONS |

Figure 1.2: A schematic representation of the Standard Model [2] of particles. The table shows the three generations of fermions (classified as quarks and leptons) that are the building blocks of all known matter in the Universe, and bosons that mediate interactions, and are thus responsible for 'forces'

The Standard Model addresses three of the four fundamental forces; it does not address the Gravitational force. The strong, weak and electromagnetic forces can be described by the $SU(3) \times SU(2) \times U(1)$ local gauge symmetry group, where the $SU(3)$ symmetry group describes the strong interaction, and the electroweak interactions are based on the $SU(2) \times U(1)$ symmetry group. There are $8+3+1$ generators associated with this model, each generator corresponding to a vector boson.

Thus, there are 8 gluons, which are massless spin 1 particles with an intrinsic property called color charge, that mediate strong interactions (described by Quantum Chromodynamics). They are respon-

sible for interactions between quarks (leptons do not interact via the strong force) as quarks have a non vanishing color charge. At low energies, quarks cannot be found in isolation, instead occurring in triplets called *Baryons*, such as protons, or a bound quark-antiquark pair, called *Mesons*. This is because of color confinement [3].

The interaction of the scalar Higgs field with the vector fields W^+ , W^- , W^0 and B causes the spontaneous breaking of the $SU(2) \times U(1)$ symmetry, resulting in 3 massive and one massless gauge boson. It also implies the existence of a neutral scalar boson, known as the Higgs boson, which was discovered in July 2012 [4]. The generators of $SU(2) \times U(1)$ correspond to the W^+, W^- and Z bosons, massive vector bosons (spin 1) that mediate weak interactions, and the massless vector boson γ (photon), which mediates electromagnetic interactions. The W bosons are charged, whereas the Z boson and γ are neutral.

1.2 Inadequacies of the Standard Model

Despite its immense success, the Standard Model does not paint a complete picture of everything that we observe. It does not account for several phenomena that are experimentally observed, such as:

- Gravity: The Standard Model does not include gravity. If, analogous to the other forces, a 'graviton' is introduced into the Standard Model as an extension, it does not describe what is observed experimentally. In fact, the Standard Model is incompatible with general relativity [5].
- Dark Matter and Dark Energy: Cosmological observations, such as galaxy rotation curves, do not match predictions based on the visible amount of mass in the universe. A fit with the observations predicts additional invisible matter, called Dark Matter [6]. Similarly, the universe is expanding at an accelerating rate, which hints at the existence of Dark Energy [7]. The Standard Model does not account for exotic matter such as these. In fact, the Standard Model only accounts for about 4% of the content of the universe [8, 9].
- Neutrino masses: Neutrinos are assumed to be massless in the Standard Model. However, neutrino oscillations have recently been observed [10], which is only possible if neutrinos have mass [11].
- Matter-antimatter asymmetry: According to the Standard Model, matter and antimatter should be created in equal quantities. However, the universe appears to have a preference for matter, indicating that in its initial state of the universe, this symmetry was broken [12].
- Hierarchy problem [13–16]: Quantum corrections to the Higgs mass are divergent, and force it to be very large. However, experiments show a surprisingly small number for the Higgs mass, at 125 GeV. There appear to be some extraordinary fine tuned cancellations that make this mass so small.

The Standard Model is incomplete, and thus requires modifications or additions to it, which are collectively called Beyond Standard Model (BSM) theories.

1.2.1 Beyond the Standard Model

Several extensions to the Standard Model have been proposed that attempt to address some of its inadequacies.

Supersymmetry (SUSY) attempts to reconcile gravity with the SM, and adds another symmetry to the Standard Model, predicting the existence of *supersymmetric* partners, called sparticles, to Standard Model particles. For example, sleptons are supersymmetric partners to the corresponding leptons, and differ by spin 1/2. SUSY would also resolve the hierarchy problem by ensuring that the divergences

would cancel out at all orders in the perturbation expansions, if the superpartners have mass near the electroweak scale (broadly, between 100 and 1000 GeV).

The observation of neutrino oscillations imply that neutrinos have mass, however, these observations can only reveal the mass difference between the different neutrino flavors. The absolute mass of the neutrinos has been constrained to have an upper limit of 2 eV, much smaller than the lightest SM particles, by precision measurements of tritium decays. To incorporate neutrino masses, an extension to the Standard Model, the see-saw mechanism, introduces right handed neutrinos and couples them to left-handed neutrinos with a Dirac mass term.

Both SUSY and the addition of a sterile right-handed neutrino to the SM are extensions that provide candidates for Dark Matter. These candidates are known as Weakly Interacting Massive Particles (WIMPs). They do not interact electromagnetically, and are thus invisible to most detectors.

1.2.2 Dark Matter

Cosmological observations of galaxies made over the decades, such as the velocity curves of galaxies (called galaxy rotation curves) indicate an anomaly; the stars in the arms of spiral galaxies appear to move faster than what would be expected from Keplerian relations, using the visible mass from the galaxies. Figure 1.3 shows the two rotation curves, expected and observed, of NGC 6503, a field¹ spiral galaxy. [17]

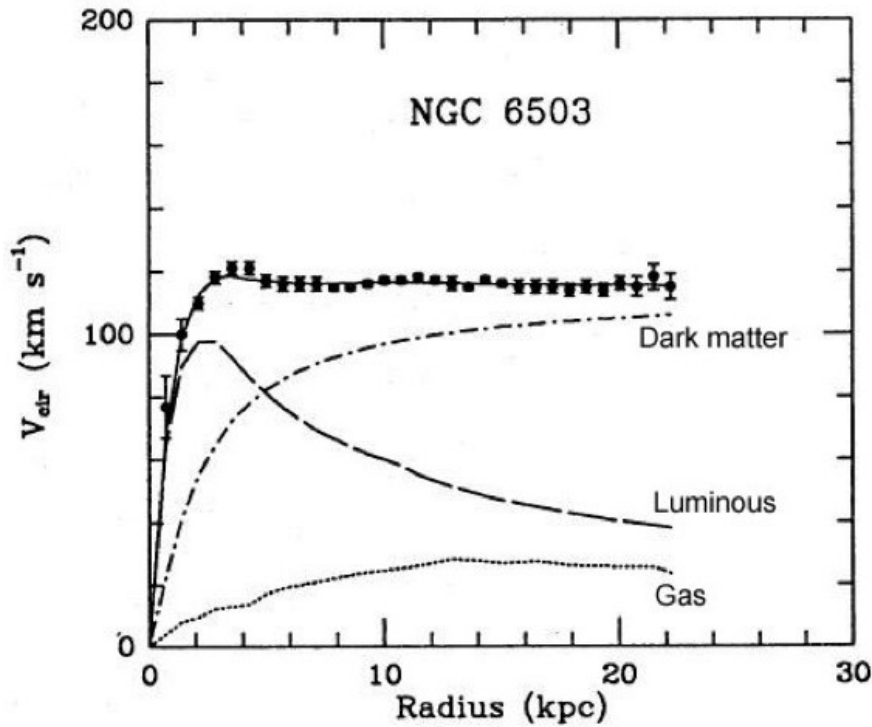


Figure 1.3: Velocity of stars in NGC 6503, a field spiral galaxy, as a function of radial distance from the center of the galaxy [17]. The 'Luminous' curve is what would be expected from the visible mass, but what is observed is much higher, indicating excess invisible matter.

Either the current understanding of Newtonian Mechanics is incomplete, or there is additional mass that is not visible which is contributing to the mass term in Newton's equation. This invisible mass is what is termed as Dark Matter. Ergo, Dark Matter appears to interact gravitationally, but not electromagnetically, with visible (Standard Model) matter. It is possible that Dark Matter is made

¹Field galaxies do not belong to a large cluster, and are thus gravitationally isolated

up of and exotic and hitherto undiscovered kind of matter, and searches are underway at the LHC to look for Dark Matter via its interactions with the Standard Model.

There is additional cosmological evidence supporting Dark Matter, such as gravitational lensing of distant galaxies, structure formation in the early universe, anisotropy in the cosmic microwave background, etc.

Dark Matter searches at the Large Hadron Collider

As Dark Matter does not interact electromagnetically, any Dark Matter particles produced in collider experiments will be invisible to detectors at the LHC. Thus, in event reconstruction, such events are expected to be marked by a significant imbalance in transverse momentum (E_T^{miss}). Currently, Dark Matter searches are conducted at the LHC [18]. Dark Matter particles are denoted by χ .

- Mono χ searches : These searches look for the production of a Standard Model particle in association with E_T^{miss} . Figure 1.4 shows the Feynman diagrams for the Mono-X processes.
 - Mono-jet : In theory, it is possible to produce Dark Matter particles in association with one or more QCD jets from initial state radiation. Thus mono-jet searches look for one or more jets in events with large E_T^{miss} .
 - Mono-V : In a similar manner to mono-jet searches, a mono-V search looks for a single vector (γ, W or Z) boson. If DM particles couple directly to a pair of gauge bosons, this may be the dominant mode of DM production.
 - Mono-Higgs : It may also be that a single Higgs boson is produced in association with E_T^{miss} . Such events would be characterised by a $H \rightarrow \gamma\gamma$ or $H \rightarrow b\bar{b}$ final state.

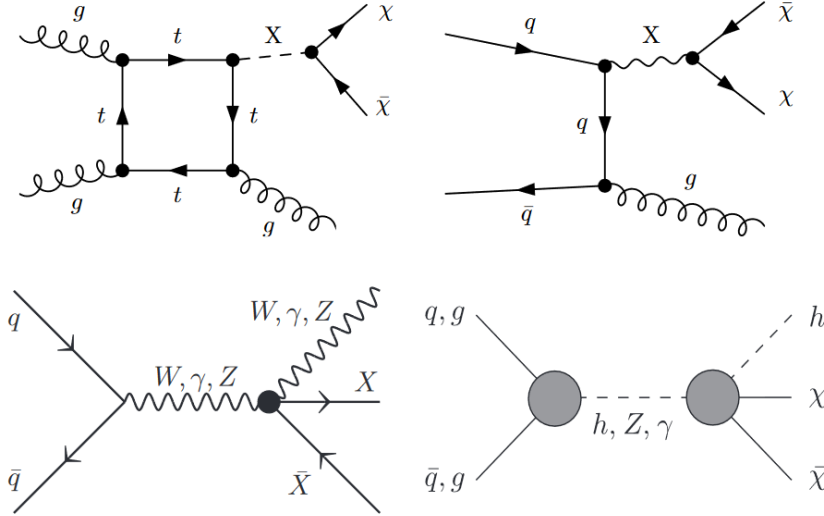


Figure 1.4: Feynman diagrams for mono X processes, showing mono-jet production (top) induced by gluons (top left) and quarks (top right) [19] where the mediator X can be a scalar, pseudo-scalar, vector or axial-vector particle; mono-V (bottom left) [20]; and mono-higgs (bottom right) [21], where h is the Standard Model Higgs boson with mass 125 GeV.

- DM+top : If DM particles couple predominantly to heavy quark flavors, a search for a top quark pair is a promising direction to head in.
- Invisible Higgs : If the mass of the DM particles is less than half the mass of the Higgs boson, it may be possible that the DM particles couple to the Standard Model via the Higgs boson, i.e $H \rightarrow \chi\chi$ processes. The main methods of Standard Model Higgs production are shown in Figure 1.1.

- Vector boson fusion (VBF): In VBF processes, the Higgs is produced from the interaction of two vector bosons.
- Production of Higgs in association with a massive vector boson (VH) : This mechanism, together with VBF are the most important methods of Higgs production in invisible Higgs searches. Such events can be recognised with a large imbalance in transverse momentum, as well as the decay products of the vector boson.
- Gluon gluon fusion (ggF) : It is also possible for the Higgs to be produced from the interaction of gluons.

This thesis investigates the Standard Model background to the $ll+E_T^{miss}$ signal with respect to the production of an invisible Higgs in association with a leptonically decaying gauge boson. Chapter 2 gives an overview of the Large Hadron Collider, the ATLAS detector, and details the event topology. Chapter 3 address the theoretical framework of this thesis.

Chapter 2

The Large Hadron Collider

The Large Hadron Collider (LHC) is a circular collider experiment located in France and Switzerland. It was built by the European Council for Nuclear Research (CERN) in collaboration with over 10000 scientists from all over the world, between 1998 to 2008, when it began its operation and started collecting data. It is the world's largest, most powerful particle collider, focusing primarily on proton-proton collisions, but also conducts heavy ion collision experiments as well. It is the largest single machine in the world.

The goal of the LHC is to experimentally test predictions made by theories of particle physics, and look for evidence of new physics. It has enjoyed remarkable successes, such as the discovery of the Higgs Boson in 2012.

The LHC houses seven experiments: ATLAS and CMS are the largest, general-purpose detectors that focus on the Higgs boson, and search for evidence new physics. ALICE is a heavy ion collider experiment that studies quark-gluon plasma, while LHCb studies CP violation. In addition, three smaller experiments, TOTEM, MoEDAL and LHCf are much smaller and used for highly specialized research.

2.1 History

The concept of the LHC was officially recognized during a workshop held by CERN and the European Committee for Future Accelerators (ECFA) during 21-27 March 1984. The tunnel that would later house the LHC was constructed between 1983-1988 to house the Large Electron-Positron Collider. The tunnel is 27 km in circumference, and located underground, underneath the Swiss-France border.

The construction of the LHC was completed in 2008, and on the 10th of September 2008, a beam of protons was successfully steered around the 27 kilometer ring of the LHC for the first time. After initial lower energy collision runs in 2009, the first 7 TeV center of mass energy collisions were recorded by the ATLAS detector in 2010.

Since then, the LHC has gone on to make remarkable discoveries. In May 2011, ALICE reported the creation of quark-gluon plasma, and extremely dense state of matter. On July 4th 2012, CERN reported the observation of a particle having mass 125 GeV, consistent with the properties of the Higgs boson. Both ATLAS and CMS teams confirmed this discovery with a statistical significance of 5 sigma, meeting the requirements to announce a new particle. The LHCb experiment observed multiple exotic hadrons, such as pentaquarks.

2.2 Design

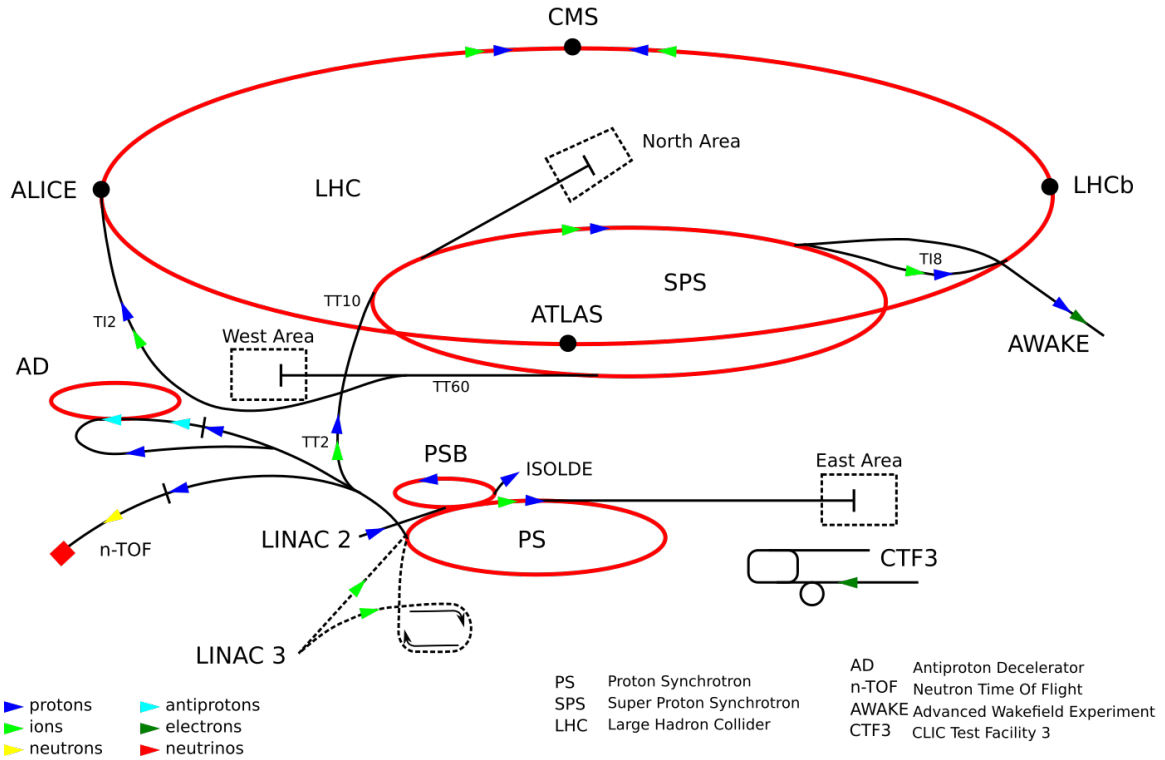


Figure 2.1: The CERN accelerator complex showing the various components of the Large Hadron Collider experiment, such as the linear accelerators, the accelerating synchrotrons, the main ring, and the four detectors, where the protons or heavy ions are collided.

Note: This section is, with minor rephrasing, taken from Wikipedia. I have to change the wording better or it'll trip plagiarism checks. For now, this section is so I have an idea of the layout and matter of this chapter.

The LHC is contained in a circular tunnel 26.7 km in circumference, located at a depth ranging between 50 and 175 meters underneath the Swiss-France border. The tunnel contains two parallel beam pipes. Each of the two beam pipes house a beam of protons (or heavy ions), which travel in opposite directions, until they are made to collide at 4 points where the beam pipes intersect. The beams are kept on their path by an array of 1232 superconducting dipole magnets. An additional 392 superconducting quadrupole magnets focus the beams to maximize the chance of interaction. Magnets of higher multipole orders are used to correct deviations in the field geometry. In total, the LHC uses about 10000 superconducting magnets. In order to keep these magnets at superconducting temperatures (-271.25°C), about 96 tonnes of helium-4 coolant is required, thus making the LHC the world's largest cryogenic facility at liquid helium temperature.

The LHC currently imparts an energy of 6.5 TeV per proton in the center of mass frame. This corresponds to velocity of about 0.999999990 c, only 3.1 m/s slower than the speed of light. At these speeds, a proton can cover the 27 km circumference of the main LHC ring in only 90 microseconds.

The colliding protons are prepared for collisions by a sequence of systems that progressively increase their energy. The linear particle accelerator, LINAC 2 generates 50 MeV protons, which are fed into the Proton Synchrotron Booster (PSB). The PSB accelerates the protons to 1.4 GeV, and from there the protons are injected into the Proton Synchrotron (PS), where they are accelerated to 26 GeV. The Super Proton Synchrotron (SPS) then increases their energy further to 450 GeV, before the protons are injected into the main ring.

Instead of a continuous beam, the protons are accumulated into bunches and accelerated to their peak

energy at 6.5 TeV over a period of 20 minutes, during which the magnetic field of the superconducting dipole magnets is increased from 0.54 to 7.7 Teslas, and circulated for up to 24 hours while collisions occur at the four intersection points. Each proton bunch consists of approximate 115 billion protons in each bunch, with about 2,800 bunches at a time. The interactions happen at intervals 25 nanoseconds apart. Figure 2.1 shows the layout of the LHC main ring, LINAC2, PSB, PS and SPS.

While LHC experiments mainly consist of proton proton collisions, for shorter times of the order of a month per year, heavy ion collisions, such as lead, are also conducted. The lead ions are first accelerated by the LINAC3 linear accelerator, an the Low Energy Ion Ring (LEIR) is used as an ion storage and cooler unit. These ions are further accelerated by the PS and SPS before being injected into the LHC main ring, where they are imparted an energy of 2.3 TeV per nucleon. The ALICE experiment is where these ions collide, in order to investigate quark-gluon plasma.

2.3 The ATLAS experiment

The ATLAS (A large ToroidaL ApparatuS¹) detector is located at one of the four beam intersection points. It is a multipurpose experiment which, after the discovery of the Higgs boson in 2012, focuses on searches for new physics, such as supersymmetry, or dark matter. The experiment is a collaboration between around 3000 physicists from over 175 institutions in 38 countries.

The ATLAS detector is a large apparatus with a cylindrical geometry, forward-backward symmetry, and nearly 4π solid angle coverage. It is 46 meters long, 25 meters in diameter and weight 7000 tonnes. The detectors consists of concentric cylindrical layers around the interaction point, where the proton beams collide. Broadly, it consists of the Inner Detector, the electromagnetic (EM) and hadronic calorimeters.

Note: Incomplete. I will complete the description of the detector, and the dimensions of the components. I will also discuss proton proton collisions, followed by the detection of particles at different components, and then triggers and data collection.

¹Sometimes, scientists are just bad at anagrams

Chapter 3

Theoretical Aspects

3.1 Invisible Higgs in association with a Z boson - ZH

In this thesis, the production of the Higgs boson, in association with a Z boson is considered. In this model, as shown in Figure 3.1, the Higgs boson mediates the interaction between Dark Matter particles and Standard Model particles, and the Z boson decays into a lepton-antilepton pair. As Dark Matter is invisible to current detectors, this process results in the $ll + E_T^{miss}$ signature.

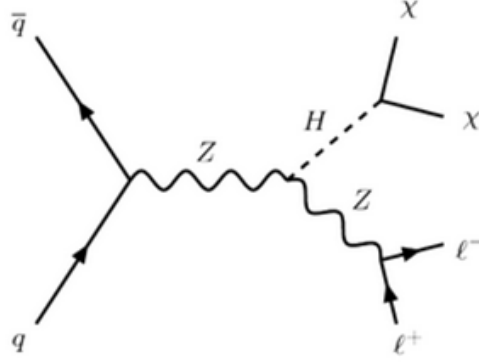


Figure 3.1: Feynman diagram showing the associated production of a Higgs boson with a Z boson. The Higgs boson decays to two invisible DM particles and the Z boson decays leptonically, resulting in the $ll + E_T^{miss}$ signature.

The main Standard Model background processes for the $ll + E_T^{miss}$ final state are $ZZ \rightarrow ll\nu\nu$, $WZ \rightarrow ll\nu$, $WW \rightarrow l\nu l\nu$, $Z + \text{jets}$ and $W + \text{jets}$.

3.1.1 Selection Criteria

The selection criteria used in Ref [22] is applied for the analysis reported in this thesis as well. The search is conducted on events with a $ll + E_T^{miss}$ final state, having a pair of high p_T electrons (ee) or muons ($\mu\mu$), and large missing transverse momentum. Events with extra leptons or b -jets are removed to reduce backgrounds, and the requirement of a boosted Z boson back to back with the missing transverse momentum vector is imposed.

Electron candidates are selected based on the ATLAS tracker and EM calorimeter dimensions, with $p_T > 7$ GeV and pseudorapidity $|\eta| < 2.47$. Similarly, muon candidates are required to have $p_T > 7$ GeV and pseudorapidity $|\eta| < 2.5$. To suppress cosmic-ray and non-prompt contributions, the longitudinal impact parameter of the leptons, $|b| < 0.5$ mm, and the transverse impact parameter divided by its error must be less than 5 for electrons and 3 for muons. To remove jets misidentified

as leptons, or leptons from b -hadron decays, 'loose' isolation criteria [?, ?] are applied. To maintain a uniform efficiency of 99% for signal leptons, the isolation selection varies as a function of p_T .

Need to add some more information about the selection criteria, with references.

Table 3.1 summarises the event selection criteria in the $ll+E_T^{miss}$ search, as shown in [22].

| Selection criteria | |
|---|--|
| Two leptons | Two opposite-sign leptons, leading (subleading) $p_T > 30$ (20) GeV |
| Third lepton veto | Veto events if any additional lepton with $p_T > 7$ GeV |
| m_{ll} | $76 < m_{ll} < 106$ GeV |
| E_T^{miss} and E_T^{miss}/H_T | $E_T^{miss} > 90$ GeV and $E_T^{miss}/H_T > 0.6$ |
| $\Delta\phi(\vec{p}_T^l, \vec{E}_T^{miss})$ | $\Delta\phi(\vec{p}_T^l, \vec{E}_T^{miss}) > 2.7$ radians |
| ΔR_{ll} | $\Delta R_{ll} < 1.8$ |
| Fractional p_T difference | $ p_T^l - p_T^{miss,jets} /p_T^l < 0.2$ |
| b -jet veto | $N(b\text{-jets}) = 0$ with b -jet $p_T > 20$ GeV and $ \eta < 2.5$ |

Table 3.1: Event selection criteria in the $ll+E_T^{miss}$ search as shown in Ref [22]

3.1.2 Results of the ZH search

As discussed in Ref [22], an upper limit of 67% is placed on the Higgs \rightarrow DM branching ratio at the 95% confidence level. The dominant source of background is the $ZZ \rightarrow ll\nu\nu$ process, contributing $\approx 60\%$ of the background. $WZ \rightarrow ll\nu\nu$ events, where the W boson decays into a electron or muon that escapes detection, account for 25% of the total background. $Z(\rightarrow ll)+$ jets process with misreconstructed E_T^{miss} contributes to about 8% of the total background, and non-resonant- ll processes, consisting of $t\bar{t}$, Wt , WW and $Z \rightarrow \tau\tau$ production contribute similarly. W +jets, VVV , and $t\bar{t}V(V)$ backgrounds contribute to a minor extent ($< 1\%$).

Figure 3.2 shows the observed E_T^{miss} distribution in the ee and $\mu\mu$ channels, compared to the signal and background predictions.

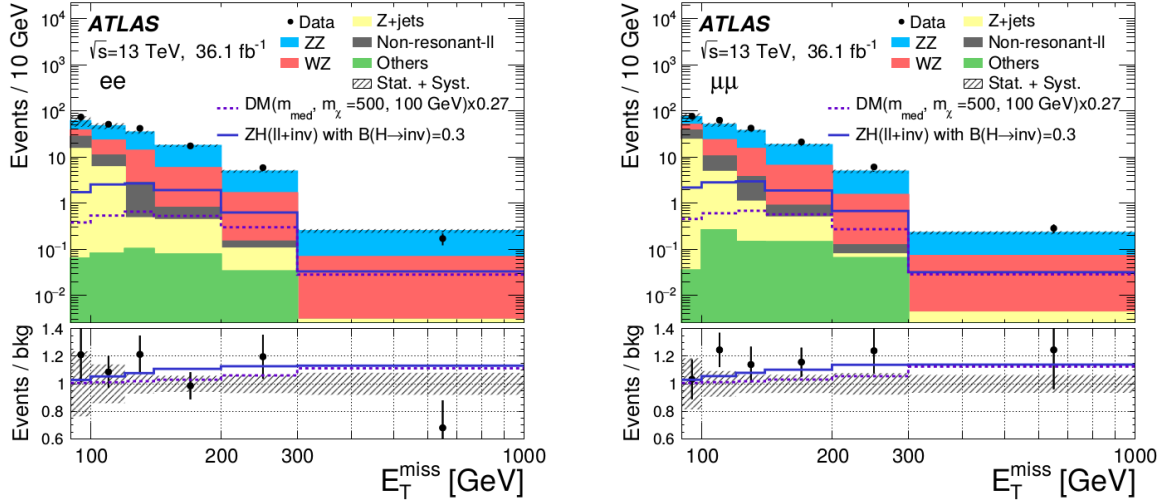


Figure 3.2: The observed E_T^{miss} distributions in the ee (left) and $\mu\mu$ channels, compared to the signal and background predictions. The total statistical and systematic uncertainty on the background predictions are shown by the error bands. The Standard Model background predictions are stacked. The $ZH \rightarrow ll + \text{invisible}$ signal distribution is shown with $B_{H \rightarrow \text{inv}} = 0.3$, and the simulated DM distribution is also scaled (with a factor of 0.27) to the best-fit contribution [22].

This thesis focuses on the ZZ background; its estimation and the uncertainty associated with it. In

Ref [22], the ZZ background is estimated from simulation, with a total uncertainty of 10%.

3.2 Background estimation: ZZ

It is difficult to identify $ZZ \rightarrow ll\nu\nu$ events, as their final state is identical to that of $ZH \rightarrow ll + E_T^{miss}$. Thus, the contribution of $ZZ \rightarrow ll\nu\nu$ is currently estimated using simulation. Figure 3.3 shows the Standard Model production of $q\bar{q} \rightarrow ZZ$ and $gg \rightarrow ZZ$. One of the Z bosons decays leptonically (into e^+e^- or $\mu^+\mu^-$), while the other Z boson decays into neutrinos ($\nu\bar{\nu}$). Neutrinos are very weakly interacting, and thus are invisible to the detectors at the LHC, and thus result in events with missing transverse momentum.

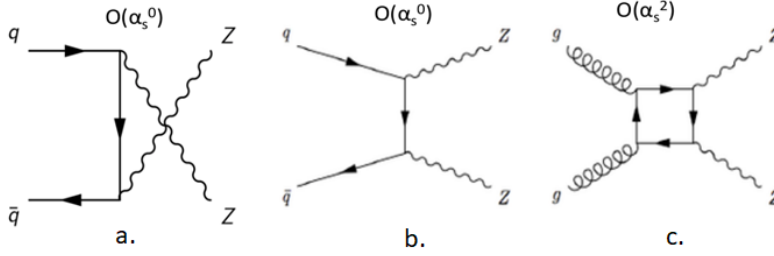


Figure 3.3: Feynman diagram showing ZZ production, in the s-channel (a) and t-channel (b) induced by $q\bar{q}$, and induced by gluons (c).

It is possible to estimate the $ZZ \rightarrow ll\nu\nu$ using $ZZ \rightarrow llll$ data. However, the precision of this process is statistically limited. The branching fraction $Z \rightarrow ll$ for one flavor of lepton (e/μ) is $\approx 3.4\%$, and $Z \rightarrow \nu\nu$ is 20%.

$$BR(ZZ \rightarrow llll) = (2 \times 0.034) \times (2 \times 0.034) = 0.00462 \quad (3.1)$$

$$BR(ZZ \rightarrow ll\nu\nu) = (2 \times 0.034) \times (0.2) \times 2 = 0.0272 \quad (3.2)$$

Thus, branching fraction of $ZZ \rightarrow llll$ ($\approx 0.46\%$) compared to $ZZ \rightarrow ll\nu\nu$ (2.7%), which is about 6 times higher. The low branching fraction of $ZZ \rightarrow llll$ limits the statistics.

Motivated by an analysis using γ +jets to estimate Z +jets [28], an alternative method to estimate $ZZ \rightarrow ll\nu\nu$ is to look at the $Z\gamma \rightarrow ll\nu\nu$ process. Figure 3.4 shows the leading order diagrams for the production of $Z\gamma$, where the Z boson further decays leptonically. Figures 3.4.a, b and c are similar to the production of ZZ , with a photon instead of one of the Z bosons. The main differences in the two processes are the couplings of the photon and Z boson to the quarks, and the fact that photons are massless, whereas the Z boson is massive.

Figure 3.4.d gives the $ll\gamma$ final state, however, the photon is radiated off of a final state lepton, i.e. Final State Radiation (FSR). This process must be suppressed, which can be done by imposing a mass window on the reconstructed mass of the two leptons to be within 15 GeV of Z boson mass shell.

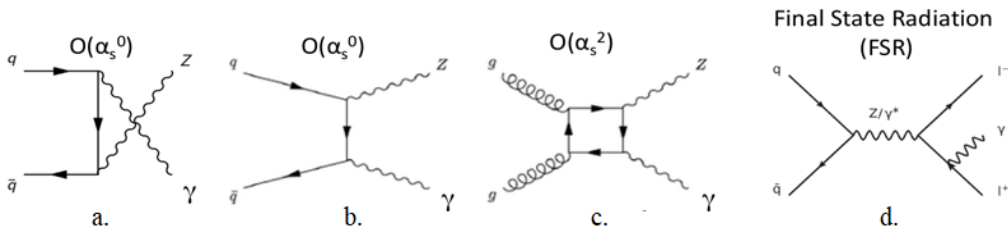


Figure 3.4: Feynman diagram showing $Z\gamma$ production, in the s-channel (a) and t-channel (b) induced by $q\bar{q}$, and induced by gluons (c). Diagram (d) shows a similar final state, but the photon is radiated off of a final state lepton (Final State Radiation).

At high Z boson transverse momentum, the $Z\gamma \rightarrow ll\gamma$ process should be kinematically similar to $ZZ \rightarrow ll\nu\nu$, as the mass of the Z boson will be negligibly small compared to its p_T . The $Z\gamma \rightarrow ll\gamma$ signal is also pure, and has a $\text{BR} \times \sigma$ as compared to $ZZ \rightarrow ll\nu\nu$. Thus, it should be possible to use $Z\gamma \rightarrow ll\gamma$ data to estimate the contribution of $ZZ \rightarrow ll\nu\nu$ in regions of high Z boson p_T .

3.3 Transfer factor R

To estimate the background, a transfer factor $R(p_T)$ is introduced, defined to be the ratio of the cross sections of $ZZ \rightarrow ll\nu\nu$ to $Z\gamma \rightarrow ll\gamma$ as a function of the p_T .

$$R(p_T) = \frac{\sigma_{ZZ}(p_T)}{\sigma_{Z\gamma}(p_T)} \quad (3.3)$$

With the two processes being kinematically similar at high p_T , R depends on the coupling of the Z and γ to quarks. It would be expected to reach a constant value at high p_T that can be determined theoretically. In the following paragraph, an attempt is made to obtain a simple approximate calculation of R from the contribution of qq process.

The photon - quark and Z boson - quark couplings in the Standard Model are given by,

$$-ieQ_q\gamma^\mu \quad \text{and} \quad \frac{-ie}{2\sin\theta_W\cos\theta_W}\gamma^\mu(v_q - a_q\gamma_5) \quad (3.4)$$

respectively, where Q_q, v_q and a_q are respectively the electric, vector and axial neutral weak couplings of the quarks, and θ_W is the weak mixing angle. There is a contribution due to the Z mass which appears in the internal propagators and phase space integration. This contribution becomes less important in the $p_T(\gamma) \gg M_Z$ region.

Thus, the leading order contributions from $q\bar{q} \rightarrow ZZ$ and $q\bar{q} \rightarrow Z\gamma$ are shown in Equation 3.5.

$$\begin{aligned} \sigma(q\bar{q} \rightarrow ZZ) &\propto \frac{1}{2} \frac{e^4 \{(v_q^2 + a_q^2)^2 + 4v_q^2 a_q^2\}}{16\sin^4\theta_W \cos^4\theta_W} \\ \sigma(q\bar{q} \rightarrow Z\gamma) &\propto \frac{e^2 Q_q^2 (v_q^2 + a_q^2)}{4\sin^2\theta_W \cos\theta_W} \end{aligned} \quad (3.5)$$

The u and d quarks present in a pp collision have different coupling strengths to the Z boson as stated in Ref [29], their relative contributions are accounted for using Equation 3.6

$$R = \frac{\sigma(u\bar{u} \rightarrow ZZ)\langle u \rangle + \sigma(d\bar{d} \rightarrow ZZ)\langle d \rangle}{\sigma(u\bar{u} \rightarrow Z\gamma)\langle u \rangle + \sigma(d\bar{d} \rightarrow Z\gamma)\langle d \rangle} \quad (3.6)$$

Using the vector and axial couplings of the Z boson to u and d quarks¹, assuming $\langle d \rangle / \langle u \rangle = 0.5$ and setting $\sin^2\theta_W = 0.2315$, $R \approx 1.28$ for the dominant $q\bar{q}$ interaction. This approximate calculation has not been performed for gluon induced channels, as they involve loops and require a more involved calculation.

This transfer factor R may be used with $Z\gamma$ data to estimate the contribution of ZZ with reasonable accuracy at high p_T . To improve precision, it is necessary to estimate the theoretical uncertainties on the transfer factor R .

3.4 Theoretical Uncertainties

In this study, the following sources of theoretical uncertainties are studied.

¹Vector and Axial couplings of Z to u and d quarks: $v_u = 0.18, a_u = 0.50, v_d = -0.35, a_d = -0.514$

- Missing higher order corrections: Contributions due to higher order QCD corrections cannot be calculated to arbitrarily high order, as it gets progressively more computationally expensive. Thus, this study is limited to Next to Leading Order (NLO), and further corrections are accounted for by varying the factorization and renormalization scales.
- Uncertainties associated with Parton Distribution Functions: A proton is a baryon, and according to the Parton model [27] and is composed of three valence quarks, and several gluons. Thus, proton-proton collisions, such as in the experiments conducted at the LHC, involve the interaction of these composite quarks and gluons (partons) at very high energies. These partons carry a fraction of the proton momentum. Parton Distribution Functions (PDFs) represent this fraction of proton momentum carried by partons as probability distributions. Owing to the non-deterministic nature of this fact, this study attempts to account for this uncertainties as PDF uncertainties.
- Photon Fragmentation Uncertainties: In the $Z\gamma \rightarrow ll\gamma$ process, the signal includes a photon. However, while reconstructing the event, soft photons, or photons resulting from other fragmentation processes may be encountered. To ensure that the photon is indeed prompt, it is required to be isolated from hadronic activity (such as pion decays). This isolation is implemented experimentally in different ways. The uncertainty associated with the implementation of this isolation is estimated as photon fragmentation uncertainties.

Each of these sources are explained further in their respective sections in Chapter 4.

3.5 Approach

Thus far, it has been established that a viable method to estimate the ZZ background contribution to the $ll+E_T^{miss}$ final state is to use $Z(\rightarrow ll)\gamma$ data, where the photon models the Standard Model invisible Z boson. A transfer factor R is introduced as the ratio of the cross sections of $ZZ \rightarrow ll\nu\nu$ to $Z\gamma \rightarrow ll\gamma$. In the high Z boson p_T region, the two processes are kinematically similar, therefore the curve of the transfer factor R as a function of p_T is expected to approach a constant value. This transfer can be used to estimate the contribution of $ZZ \rightarrow ll\nu\nu$ from $Z\gamma \rightarrow ll\gamma$ data.

This thesis estimates the theoretical uncertainties on the transfer factor. The $ZZ \rightarrow ll\nu\nu$ and $Z\gamma \rightarrow ll\gamma$ cross sections are obtained from MCFM, a femtobarn level matrix element generator. Varying the input parameters provided in the MCFM input file, the theoretical uncertainties are estimated.

Chapter 4

Transfer factor R and the uncertainties associated to it

4.1 MCFM

Monte Carlo for FeMtobarn processes (MCFM) is a program that calculates cross sections for femtobarn-level processes at leading order(LO) or next to leading order (NLO) QCD. In this study, MCFM v8.0 [30–33] is used to generate cross sections of $ZZ \rightarrow ll\nu\nu$ and $Z\gamma \rightarrow ll\gamma$ processes at NLO, with a selection of generator level cuts. The generation parameters in MCFM allow fine control over the sample, such as PDF sets, photon isolation, lepton and photon p_T and η , renormalization and factorization scales, etc. The samples are generated with cuts on $E_T^{miss} = p_T(Z \rightarrow \nu\nu)$ for the ZZ process and $p_T(\gamma)$ for the $Z + \gamma$ process. A ratio of these cross sections is taken to obtain the R distribution as a function of p_T . The uncertainty on R is calculated by varying several parameters at the generator level, such as the renormalization and factorization scales, the PDF sets used, photon fragmentation, etc. The contributions of the $q\bar{q}$ and gg processes are estimated separately.

In MCFM generated events, leptonically decaying Z boson are constrained to an electron-positron pair only, i.e. $Z \rightarrow ee$. As electrons and muons have similar properties with the exception of mass, simply the branching fraction of $Z \rightarrow ee$ must be accounted for to obtain the inclusive value of R .

$$R_{inc} = R * \frac{BR(Z \rightarrow ee)}{BR(Z \rightarrow ee) * BR(Z \rightarrow \nu\nu) * 2} \quad (4.1)$$

Table 4.1 lists the generator level settings used for the ZZ and $Z + \gamma$ processes. All lepton cuts are consistent with the ones used in the ATLAS $Z + E_T^{miss}$ analysis [22], as shown in Table 3.1.

| Cuts | $ZZ \rightarrow ee\nu\nu$ | $Z(\rightarrow ee) + \gamma$ |
|------------------------------|---------------------------|------------------------------|
| Process ID | 87 | 300 |
| M_{ee} | $76 < M_{ee} < 106$ GeV | $76 < M_{ee} < 106$ GeV |
| $M_{\nu\nu}$ | - | - |
| Order | NLO | NLO |
| PDF set | CT14 | CT14 |
| $p_T^{\text{lead}}(e)$ | > 30 GeV | > 30 GeV |
| $ \eta^{\text{lead}}(e) $ | < 2.47 | < 2.47 |
| $p_T^{\text{sublead}}(e)$ | > 20 GeV | > 20 GeV |
| $ \eta^{\text{sublead}}(e) $ | < 2.47 | < 2.47 |
| $p_T(V)^*$ | > 90 GeV | > 90 GeV |

Table 4.1: Settings in input.DAT for MCFM

The constraint on M_{ee} in the case of $Z + \gamma$ suppresses the FSR process by ensuring that the lepton pair

are from a Z decay only. In addition, the renormalization and factorization scales for both processes are set to be $H_T = \sum_i p_{T,i}$. Photon isolation is implemented using the Frixione [44] method, with $R_0 = 0.4$, $\epsilon = 0.075$ and $n = 1$. These parameters are further explained in Section 4.2.3.

4.2 Preliminary Results

Using the settings listed in Table 4.1, the cross sections for $ZZ \rightarrow eev\nu$ and $Z\gamma \rightarrow ee\gamma$ are generated, as shown in Figure 4.1. Throughout this analysis, these samples are the reference.

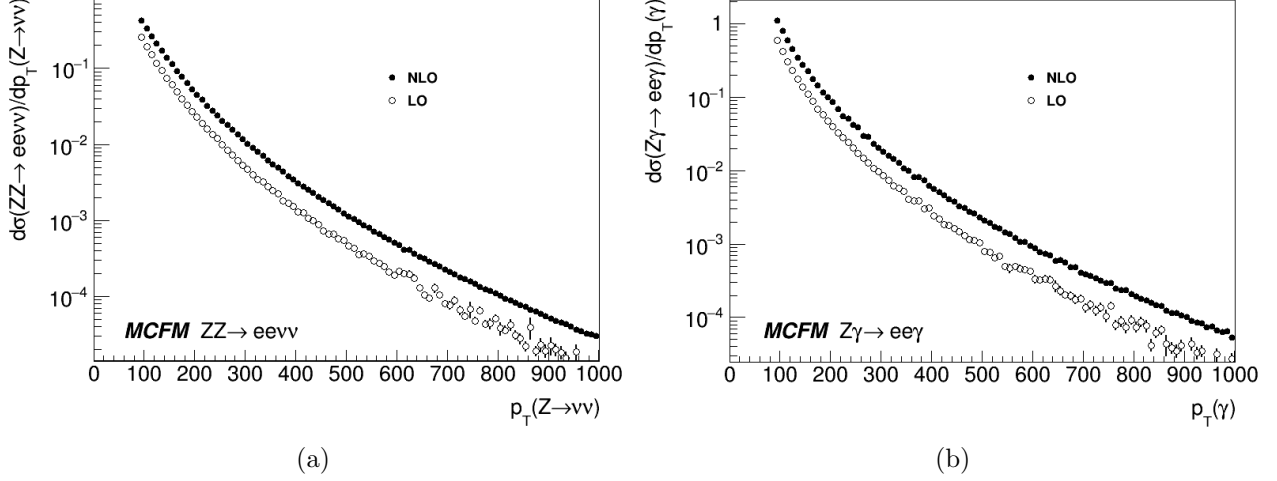


Figure 4.1: NLO and LO cross sections of $ZZ \rightarrow eev\nu$ (left) and $Z\gamma \rightarrow ee\gamma$ (right) processes with the cuts as in Table 1. The vertical axis is in \log_{10} scale. The leptonically decaying Z boson decays to an e^+e^- pair. There is no flavor constraint on the neutrinos.

The ratio $R = \sigma(ZZ \rightarrow eev\nu)/\sigma(Z\gamma \rightarrow ee\gamma)$ is shown in Figure 4.2, taken as the ratio of the cross sections in Figures 4.1a and 4.1b. Additional events are generated with E_T^{miss} and $p_T(\gamma) > 400$ GeV for the two processes respectively to increase statistics.

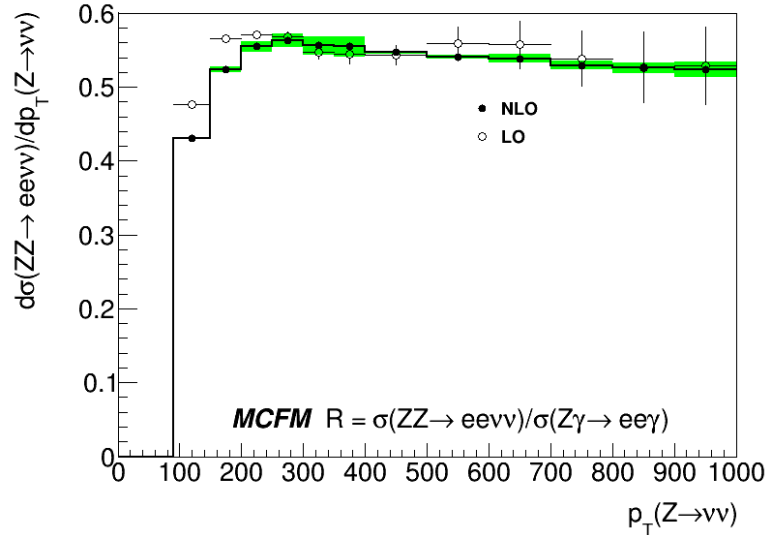


Figure 4.2: The transfer factor R as a function of p_T , taken as a ratio of the $ZZ \rightarrow eev\nu$ and $Z\gamma \rightarrow ee\gamma$ cross sections at both LO and NLO. The leptonically decaying Z boson decays to an e^+e^- pair.

* V is a vector boson: $Z(\rightarrow \nu\nu)$ for the ZZ process; γ for the $Z\gamma$ process

The R value is observed to increase from ≈ 0.39 at 50 GeV to ≈ 0.52 at high p_T , where it reaches a plateau. When the branching ratio of Z boson decaying selectively to e^+e^- , or to $\nu\nu$, is accounted for as shown in Equation 4.1, the resulting ratio $R(p_T)$ is shown in Figure 4.3, which shows the ratio of $\sigma(ZZ)$ to $\sigma(Z\gamma)$, i.e. if the Z bosons do not decay further. The value of R is observed to increase from ≈ 0.98 at 50 GeV to ≈ 1.3 at high p_T , in reasonable agreement with the simple approximate calculation presented in Chapter 3 of $R \approx 1.28$.

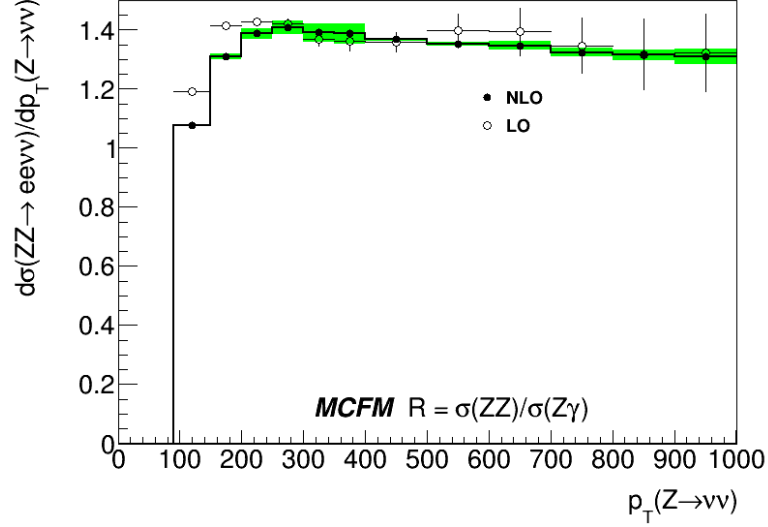


Figure 4.3: The transfer factor R as a function of p_T at both LO and NLO, adjusted for the $Z \rightarrow ee$ and $Z \rightarrow \nu\nu$ branching ratios. This shows the $R = \sigma(ZZ)/\sigma(Z\gamma)$, where the Z bosons do not decay.

Figure 4.4 shows the normalized rapidity distributions for missing transverse momentum ($Z \rightarrow \nu\nu$) and the photon respectively. The photon rapidity is restricted to $|\eta| < 2.5$.

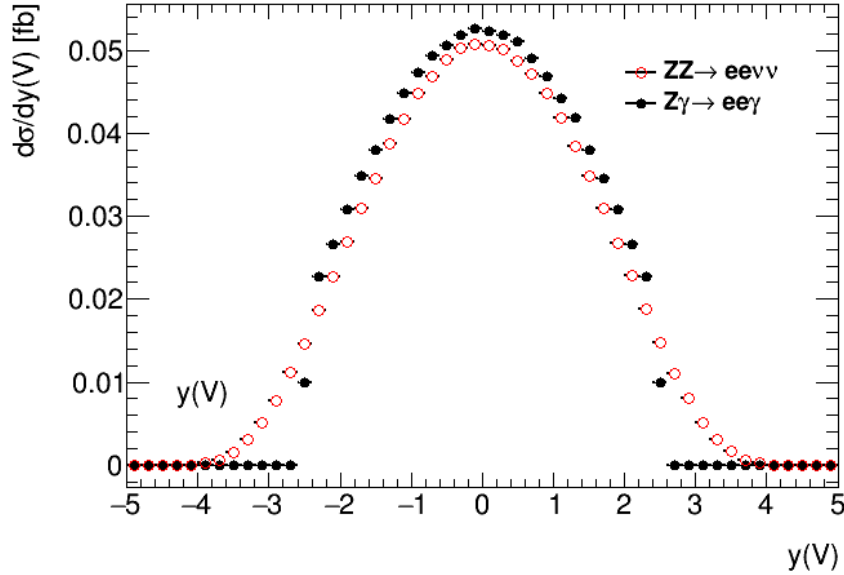


Figure 4.4: The normalized distributions showing the differential cross sections of $ZZ \rightarrow ll\nu\nu$ and $Z\gamma \rightarrow ll\gamma$ processes as a function of the rapidity of the vector boson $y(V)$ ($Z \rightarrow \nu\nu$ for $ZZ \rightarrow ll\nu\nu$, or γ for $Z\gamma \rightarrow ll\gamma$). The rapidity range for the photon is restricted to be $|\eta| < 2.5$.

Figures 4.5 and 4.6 further illustrate the topology of the events by showing normalized distributions for the leading and subleading lepton p_T and rapidity.

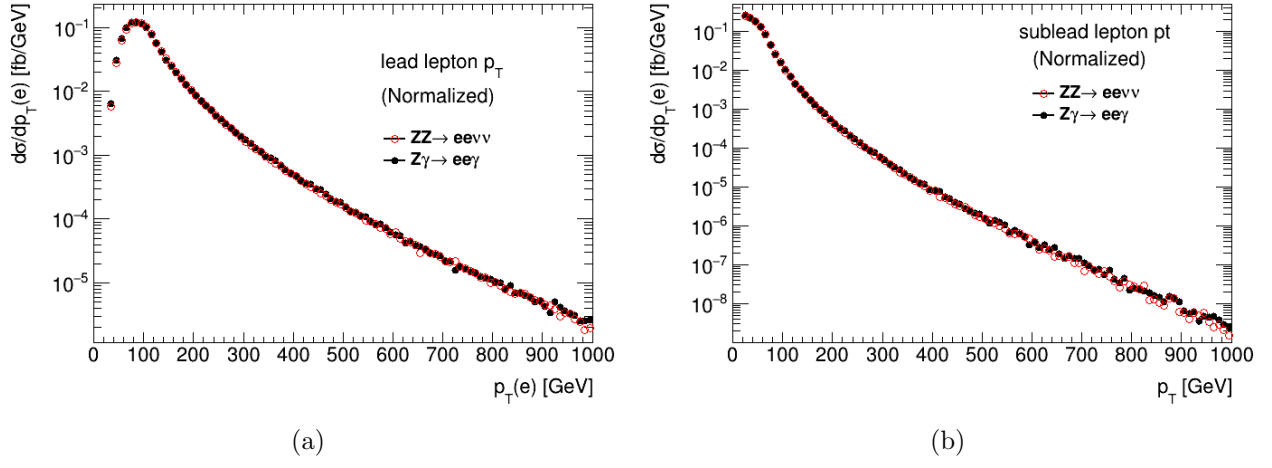


Figure 4.5: Normalized distributions showing the differential cross section as a function of the transverse momentum of the leading (left) and subleading (right) leptons for the two processes.

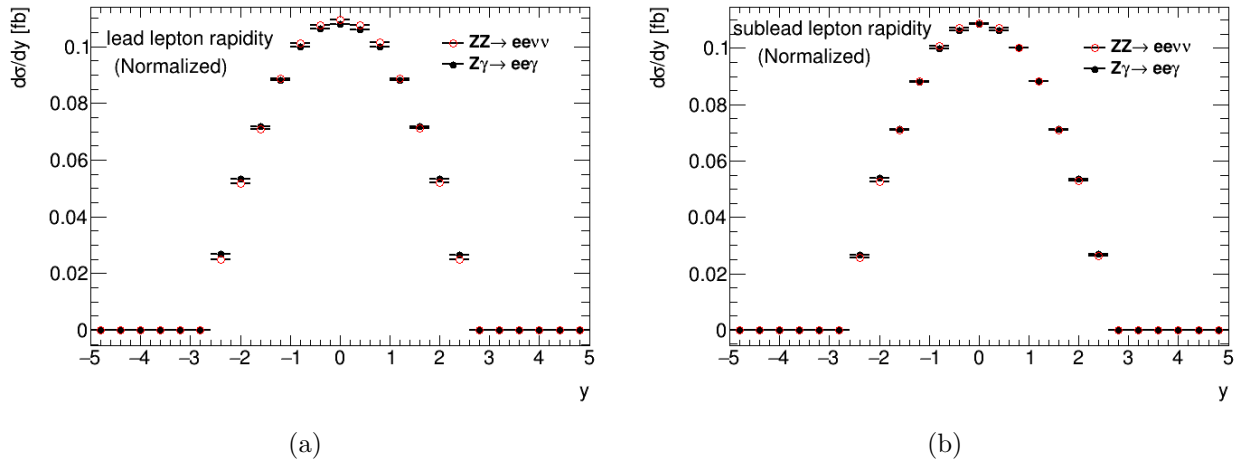


Figure 4.6: Normalized distributions showing the differential cross section as a function of the rapidity of the leading (left) and subleading (right) leptons for the two processes.

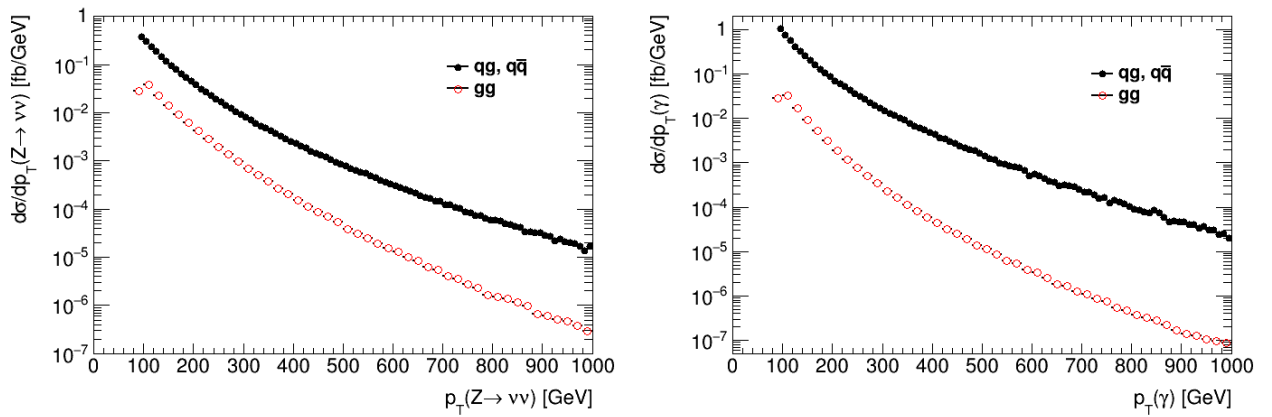


Figure 4.7: The cross sections of $ZZ \rightarrow ee\nu\nu$ (left) and $Z\gamma \rightarrow ee\gamma$ (right) as a function of p_T , from the contributing $q\bar{q}, qq$ and gg processes. The leptonically decaying Z boson decays to an electron-positron pair

Gluon-gluon processes contribute to 8.6% of the total cross section for the ZZ process and 2.5% of the $Z + \gamma$ process. As shown in Figure 4.7, the $q\bar{q} + qq$ and gg contributions to the ZZ and $Z\gamma$ cross

section, it is seen that at low p_T , gluon-gluon processes contribute more than at high p_T .

The R_{gg} distribution, shown in Figure 4.8 is observed to approach an asymptotic value at a much higher $p_T = 1.5$ TeV.

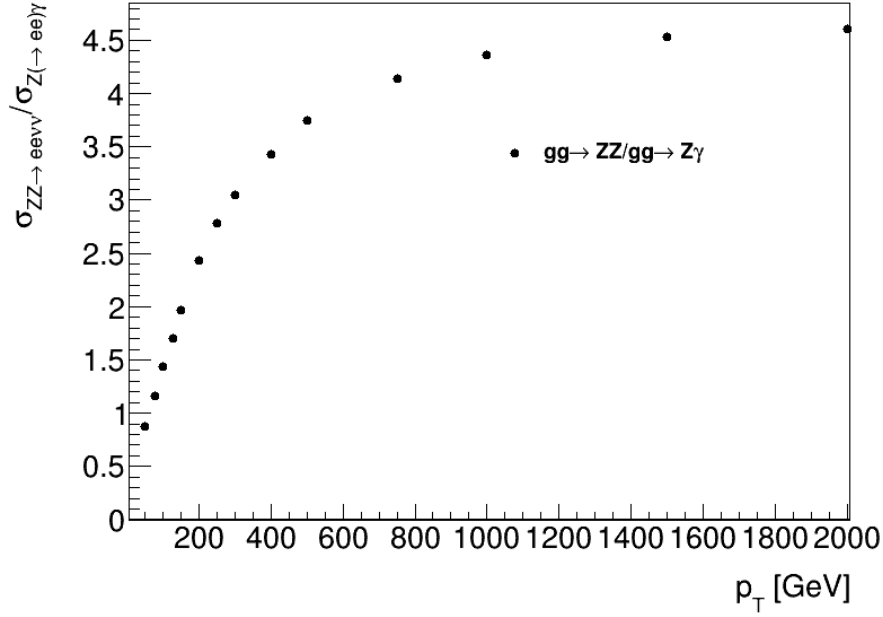


Figure 4.8: $R_{gg}(p_T)$, computed from the contributions of the gg subprocess to the cross sections of ZZ and $Z\gamma$. The curve reaches a plateau at a much higher p_T than for contributions from the $q\bar{q}$ process only. The leptonic Z bosons decay to an ee pair.

4.2.1 Uncertainty from Missing Higher Order Corrections

Note: I intend to add an appendix detailing the process of regularization and renormalization with examples. I will need to refresh my theory.

In QCD calculations, higher order perturbative corrections may be added to the vertices or propagators in a Feynman diagram. An example illustrating these 'loop' corrections is shown in Figure 4.9. Physically, these corrections occur at very small time scales. These perturbative corrections lead to divergent integrals that are progressively more difficult to calculate at higher orders. A perfect calculation, carried out up to infinite orders, would give the exact cross section. However current technological capabilities limit the order to which calculations can be carried out.



Figure 4.9: Loop corrections to the propagator and vertex illustrated using a Feynman diagram showing $\gamma \rightarrow e\nu$, for example. These loops represent interactions that happen at very small distance scales (and corresponding, very high energy scales), and are calculated perturbatively in QCD.

While calculating loop corrections, two kinds of divergences are encountered: infrared divergences, and ultraviolet divergences. Infrared divergences occur when the integral diverges due to the contributions

of particles with very low energies (or equivalently, interactions at large distances), and typically involve terms featuring $1/k$, thus diverging as $k \rightarrow 0$. Ultraviolet divergences are logarithmic divergences involving the term $\int d^4k \, 1/k^4$. Integrals of this form simplify as terms involving $\int \ln(k) dk$ that diverge as the integration variable approaches ∞ , occurring at very high energy scales, or equivalently, interactions at extremely short distances. They correspond to physics at long and short distances. Here, long distances are those where soft interactions take place, away from the hard parton-parton interaction. Short distances are those where the hard parton-parton interactions occur.

Thus, it is necessary to regularize such integrals, i.e. render the divergences finite, or have them cancel out somehow. One method of addressing these divergences is to introduce a cutoff scale Λ as the (upper or lower) limit in the momentum integrals, such as through the Pauli-Villars regularization. The divergences will then be proportional to $\log \Lambda/\mu^2$, where μ^2 is some arbitrary scale, an artifact of the regularization.

Dimensional regularization is another, more effective method of regularization, where the power of the momentum integration is shifted by an infinitesimally small amount 2ϵ , i.e. $\int d^4q/(2\pi)^4 q \dots \rightarrow \mu^{2\epsilon} \int d^{4-2\epsilon}q/(2\pi)^4 q \dots$. A prefactor $\mu^{2\epsilon}$ is introduced, where μ is an arbitrary scale, to ensure that all observables have the dimension of mass. Thus, regularization envelops the effect of these divergences into the arbitrary scale μ . Upon renormalizing these regularized integrals, the $1/\epsilon$ divergent terms cancel out, leaving only the scale μ to be addressed. In QCD calculations, this scale appears as part of a scale dependent parameter, namely the running strong coupling constant ($\alpha_s(\mu)$).

The infrared divergences are addressed by the inclusion of the factorization scale μ_F , while the ultraviolet divergences are addressed by the inclusion of the renormalization scale μ_R . These parameters are arbitrary, and are set by hand. These are then varied between $\frac{1}{2}\mu < \mu < 2\mu$ to obtain an indication of the dependence of the matrix element on the scales, and thus, the uncertainty around the chosen scale.

Perturbative QCD calculations get progressively more computationally expensive as the order of the perturbative theory increases. Thus, perturbative QCD calculations are only carried out up to a fixed order. There is a difference in the cross sections obtained from one order to the next, and thus, a contribution from the uncalculated higher perturbative orders is expected. To account for the missing higher order corrections, K -factors are introduced, defined in Equation 4.7 as the ratio of the cross section at the highest available order to the leading order cross section.

To address uncertainties associated with the scale in this study, the prescription used in Ref [35], section 4 is followed. The central scale, μ_0 is chosen to be $H_T/2$ for both $ZZ \rightarrow ll\nu\nu$ and $Z\gamma \rightarrow ll\gamma$ samples (where H_T is the scalar sum of the transverse momentum of all particles after collision, $\sum_i p_{T,i}$), and seven-point variations are applied, i.e.

$$\frac{\mu_i}{\mu_0} = (1, 1), (1, 2), (2, 1), (2, 2), (0.5, 1), (1, 0.5), (0.5, 0.5) \quad (4.2)$$

where $i = 0, \dots, 6$. The central cross section value is taken to be the mean of the maximum and minimum cross sections resulting from this variation, and the uncertainty to be the half the difference between the same.

$$\sigma_{NLO}^{(V)} = \frac{1}{2} \left[\sigma_{NLO}^{(V,max)} + \sigma_{NLO}^{(V,min)} \right] \quad (4.3)$$

$$\delta\sigma_{NLO}^{(V)} = \frac{1}{2} \left[\sigma_{NLO}^{(V,max)} - \sigma_{NLO}^{(V,min)} \right] \quad (4.4)$$

where

$$\sigma_{NLO}^{(V,max)} = \max \left\{ \sigma_{NLO}^{(V)}(p_T(V), \mu_i) | 0 \leq i \leq 6 \right\} \quad (4.5)$$

$$\sigma_{NLO}^{(V,min)} = \min \left\{ \sigma_{NLO}^{(V)}(p_T(V), \mu_i) | 0 \leq i \leq 6 \right\} \quad (4.6)$$

and $V = Z \rightarrow \nu\nu$ for $ZZ \rightarrow ll\nu\nu$, or $V = \gamma$ for $Z\gamma \rightarrow ll\gamma$. This uncertainty is propagated to R .

The two processes are kinematically similar at high p_T . Thus, naively, a cancellation of the contribution due to missing higher order corrections would be expected between the two processes due to this correlation. To estimate the degree of correlation between the processes, the process dependent part of the cross sections may be used. Since the study is undertaken at NLO, the K -factor is defined as in Equation 4.7.

$$K_{NLO}^{(V)} = \sigma_{NLO}^{(V)}(p_T)/\sigma_{LO}^{(V)}(p_T) \quad (4.7)$$

To estimate the unknown process dependent correlation effects, the difference between the K -factors of the $ZZ \rightarrow ll\nu\nu$ and $Z\gamma \rightarrow ll\gamma$ processes is taken.

$$\delta^{(2)}\sigma_{NLO} = K_{NLO}^{(\gamma)}(p_T) - K_{NLO}^{(Z)}(p_T) \quad (4.8)$$

Applying the above prescription, the variation of scales for cross sections of $ZZ \rightarrow ee\nu\nu$ and $Z\gamma \rightarrow ee\gamma$ are shown in Figure 4.10 below.

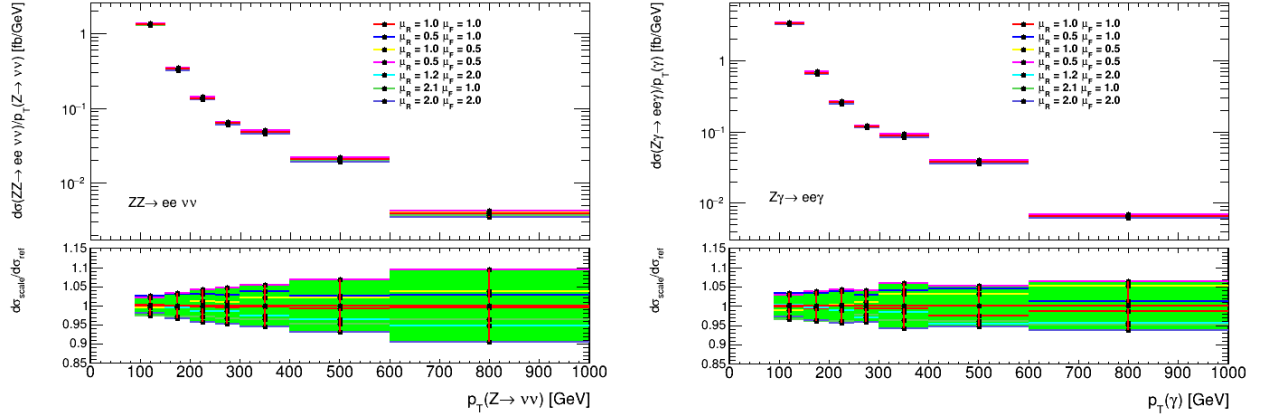


Figure 4.10: The scale variations around the cross sections of $ZZ \rightarrow ee\nu\nu$ (left) and $Z\gamma \rightarrow ee\gamma$ (right)

At 100 GeV, the deviation from the central value is about 3% for both processes and increases to 10% at high p_T . Here, the prescription in Equations 4.3 and 4.4 is used to compute the central value and uncertainty.

Treating the scales as correlated between the processes, the scale variation for the transfer factor R is shown in Figure 4.11. The central value of R and the uncertainty band around it is taken according to Equations 4.3 and 4.4 applied to R .

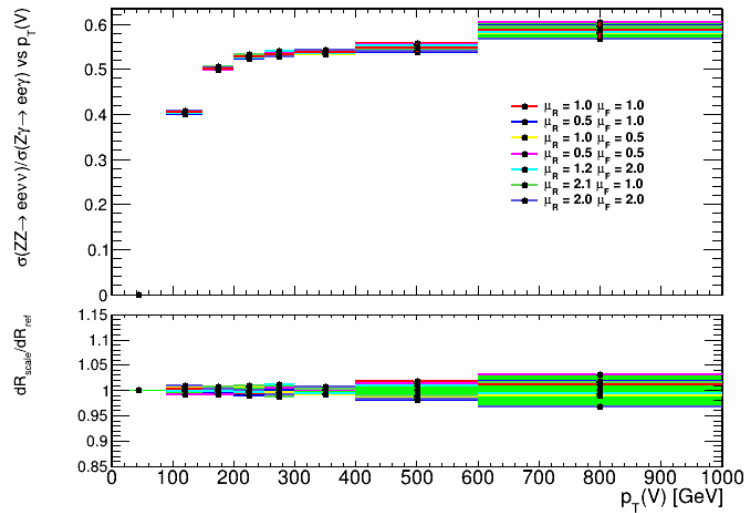


Figure 4.11: The transfer factor $R = \sigma(ZZ \rightarrow ee\nu\nu)/\sigma(Z\gamma \rightarrow ee\gamma)$ (top), with the scales varied in a correlated manner for both ZZ and $Z\gamma$ processes. The bottom plot shows the relative ratio R_i/R_0 of the varied transfer factors to the central value.

The correlated scale uncertainty around R is lower compared to that of the individual cross sections. At 100 GeV, $R \approx 0.4 \pm 0.037$, or an uncertainty of 1%. At high p_T , $R \approx 0.55 \pm 0.01$, the uncertainty is 1.8%.

To study the uncertainty due to unknown process dependent correlation effects, the K -factor study is undertaken, following the prescription in Equations 4.7 and 4.8. Figure 4.12

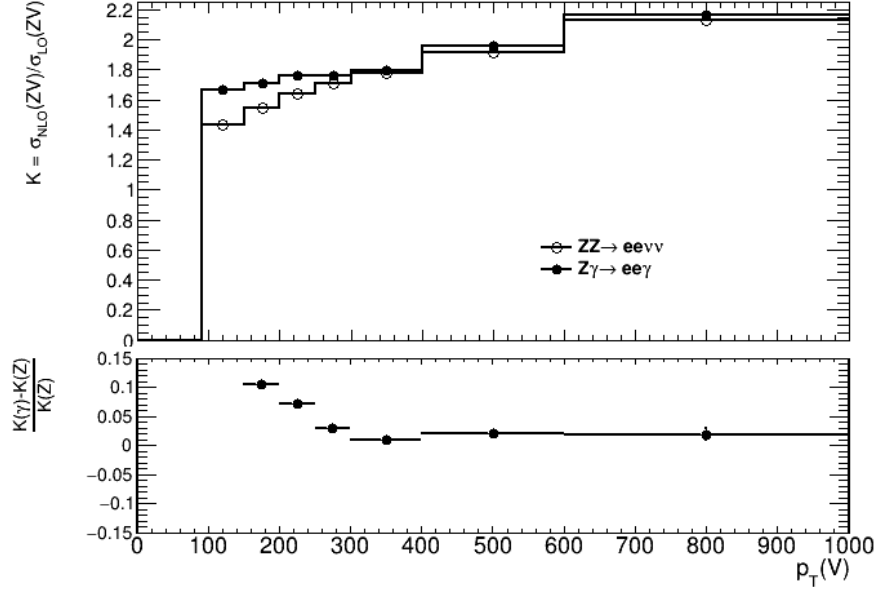


Figure 4.12: The K factor to estimate the unknown process dependent correlations, defined as $\sigma_{\text{NLO}}(V)/\sigma_{\text{LO}}(V)$. The bottom plot shows the K -factor difference relative to $K(Z)$.

4.2.2 Uncertainty associated with Parton Distribution Functions

A proton is a baryon, i.e. it is composed of quarks and several gluons. In a proton-proton collision, it is these quarks and gluons, called *partons* that actually interact. This is illustrated by Figures 3.3 and 3.4, which show the Feynman diagrams for quark-quark and gluon-gluon interactions. Thus it is important to know the momentum of the interacting partons. It is not possible to deterministically know the momentum of the partons, as it is the momentum of the protons that is set during the experiment. However, the fraction of the proton momentum that is carried by the partons can be modelled as probability distributions.

Parton Distribution Functions (PDFs) characterize the fraction of proton momentum carried by partons as probability distributions. PDF sets are collections of PDFs that model the uncertainty associated with parton momenta.

QCD predicts quantitatively the rate of change of parton distributions when the energy scale Q^2 varies, governed by the DGLAP equations [34], in the region where perturbative calculations can be applied. While the DGLAP differential equations give the energy scale Q^2 dependence, they cannot definitively predict the x dependence of the parton distributions at a given Q^2 , and must be extracted from data. Thus, PDFs sets are obtained by fitting on a large number of cross section data points, on a grid of Q^2 and x values from several experiments. This work is carried out by groups such as MSTW [38–40], MMHT [41], NNPDF [42], etc.

Note: I could discuss DGLAP equations here or in an appendix, and mention information regarding the data collections. I will also definitely add a PDF plot here.

The PDF set used for reference is the CT14 [36] PDF set. The uncertainty on the PDFs is studied by using the 30 variations provided by the PDF4LHC15 set [37], constructed from the combination of CT14, MMHT14 and NNPDF3.0 PDF sets. These sets are provided by LHAPDF6 [43]. PDF4LHC15 provides a set of variations that include those determined by different groups (MSTW, CTEQ and

NNPDF). The set used here is PDF4LHC15_nlo_30, consisting of 30 members.

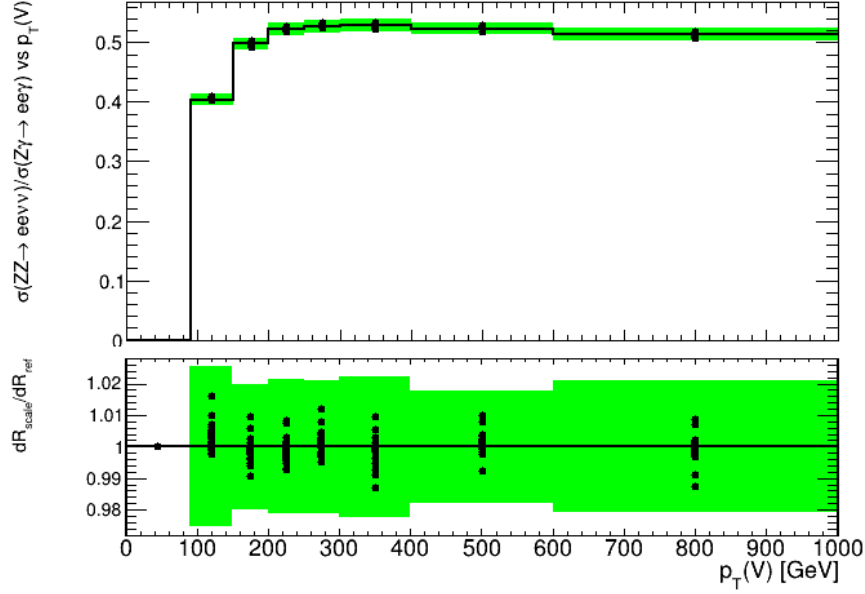


Figure 4.13: The transfer factor $R = \sigma(ZZ)/\sigma(Z\gamma)$ (top), and the relative ratio R_i/R_0 of the transfer factor calculated using PDF sets 1-30, with respect to set 0 which is taken as the central value.

Fig.4.13 shows the comparison of the ratio $R(p_T)$ from the 30 member sets of PDF4LHC15_nlo_30. To measure the uncertainty due to these 30 sets, analogous to Equation 20 in Ref [37], Equation 4.9 is used:

$$\delta^{PDF} R = \sqrt{\sum_{k=1}^{N_{mem}} (R^{(k)} - R^{(0)})^2} \quad (4.9)$$

where N_{mem} is the number of member sets in the group, in this case, 30.

The combined uncertainty around $R \approx 0.40$ is ± 0.01 , or about 2.3%, at 100 GeV. The uncertainty is about 2% at high p_T values, with $R \approx 0.51 \pm 0.01$.

4.2.3 Photon Fragmentation and Isolation Uncertainty

The $Z\gamma \rightarrow l\bar{l}\gamma$ process may contain photons that arise from the hadron showers. It is therefore important to isolate the prompt photon from hadronic activity. This reduces unwanted background from pion decays, or fragmentation processes.

Experimentally, photon isolation is implemented with the following selection:

$$\sum_{\in R_0} E_T(\text{had}) < \epsilon_h p_T^\gamma \quad \text{or} \quad \sum_{\in R_0} E_T(\text{had}) < E_T^{max} \quad (4.10)$$

limiting the transverse hadronic energy $E_T(\text{had})$ in a cone of size $R_0 = \sqrt{\Delta\eta^2 + \Delta\phi^2}$ around the photon, to some fraction of the photon p_T , or some fixed small cut-off.

The smooth cone isolation method of Frixione [44] is an alternative isolation procedure, which simplifies calculations by avoiding fragmentation contributions. The following isolation prescription is applied to the photon:

$$\sum_{R_{j\gamma} \in R_0} E_T(\text{had}) < \epsilon_h p_T^\gamma \left(\frac{1 - \cos R_{j\gamma}}{1 - \cos R_0} \right)^n. \quad (4.11)$$

where $R_{j\gamma}$ is the separation of the photon and the j^{th} hadron. This requirement constrains the sum of hadronic energy inside a cone of radius $R_{j\gamma}$, for all separations $R_{j\gamma}$ less than a chosen cone

size R_0 . This prescription allows soft radiation inside the photon cone, but collinear singularities are removed. The smooth cone isolation is infrared finite, thus fragmentation contributions do not need to be included.

The two prescriptions are significantly different. The Frixione method has its advantages, namely that it is infrared finite, removes collinear singularities and avoids fragmentation effects. However, Frixione isolation is difficult to implement experimentally, while the relative isolation, given by Equation 4.2.3 is readily used in experimental analyses. For the purpose of this analysis, the Frixione method is used, and the parameters ϵ and n are varied to get a handle on the uncertainty associated with the Frixione isolation method. In addition, the difference from the experimental isolation method is accounted for as part of the uncertainty.

In this analysis, R_0 is chosen to be 0.4 to agree with the experimental definition. The central value is chosen to be from the sample using smooth cone isolation (Frixione) with $\epsilon_h = 0.075$ and $n = 1$. These parameters are varied within a reasonable range to assess the uncertainty as shown in Figure 4.14.

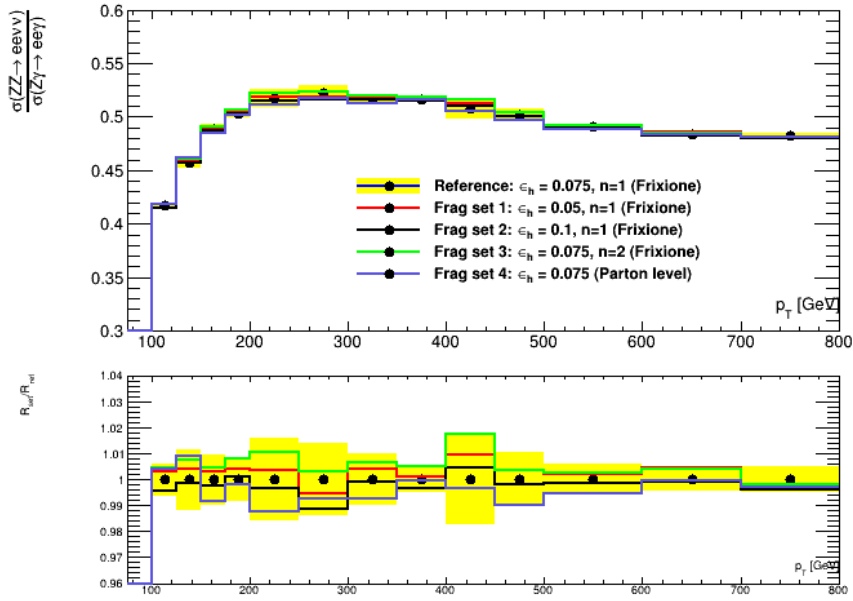


Figure 4.14: R distribution as a function of p_T , showing the uncertainty due to variation of photon isolation parameters ϵ_h and n in the smooth cone isolation procedure (Frixione), and ϵ_h in the photon isolation procedure. The lower panel shows the relative deviation of the varied sets from the central value, as well as the uncertainty band.

The uncertainty is calculated from the four sets listed in Figure 4.14:

$$\begin{aligned} \delta R_i &= |R_i - R_{ref}| & i \in (1, 2, 3, 4) \\ \delta R &= \sqrt{\max_{i=1,2,3} (\delta R_i)^2 + (\delta R_4)^2} \end{aligned} \quad (4.12)$$

as the effects assessed by changing the isolation definition in set 4, and varying the parameters in sets 1-3 are different.

The uncertainty is $< 2\%$ over the whole p_T range.

Chapter 5

Additional Figures

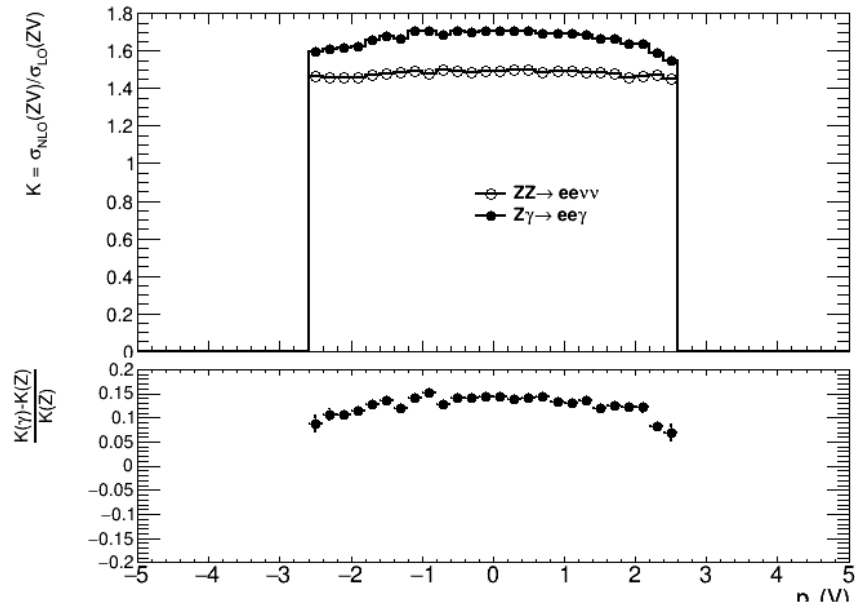


Figure 5.1: K factor as a function of rapidity

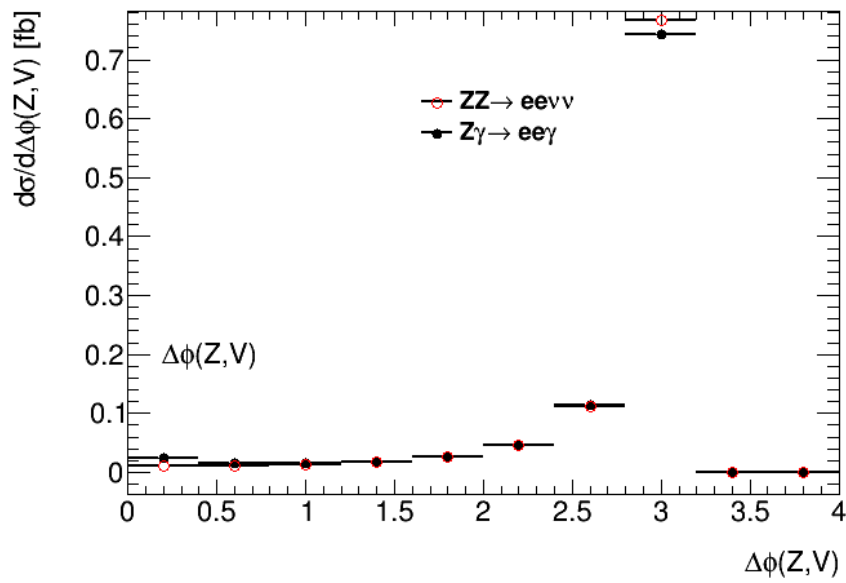


Figure 5.2: $d\phi(Z,V)$

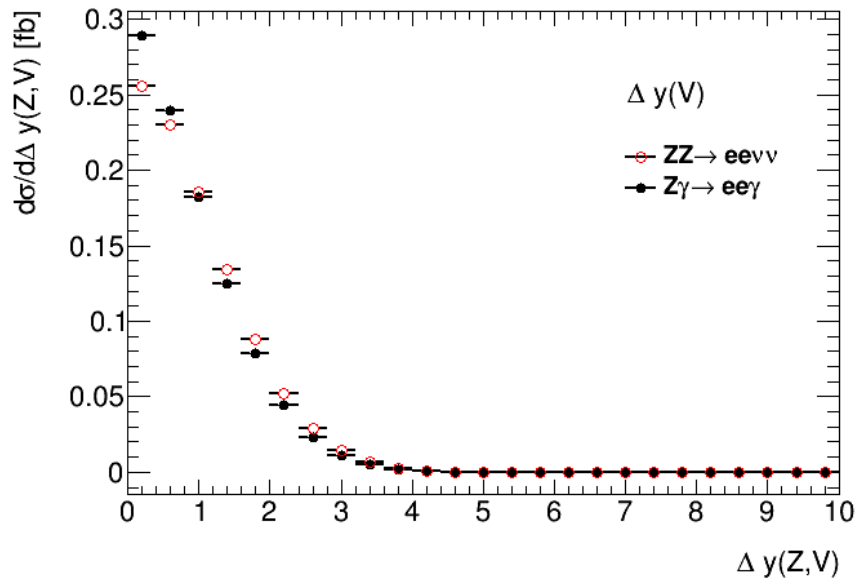


Figure 5.3: $d\sigma/d\Delta y(Z,V)$
Matter and Antimatter in the Universe

Bibliography

- [1] **D. J. Griffiths**, Introduction to Elementary Particles 2nd Edition, 2004 WILEY-VCH Verlag GmbH & Co. KGaA, Weinheim
- [2] PBS NOVA, Fermilab, Office of Science, United States Department of Energy, Particle Data Group.
- [3] **J. Greensite (2011)**. An introduction to the confinement problem. Springer. ISBN 978-3-642-14381-6.
- [4] **ATLAS Collaboration**, Observation of a New Particle in the Search for the Standard Model Higgs boson with the ATLAS detector at the LHC, Phys.Lett. B716 (2012) 1-29, [arXiv:1207.7214 \[hep-ex\]](#)
- [5] **A. O. Sushkov, W. J. Kim, D. A. R. Dalvit, S. K. Lamoreaux**, New experimental limits on non-Newtonian forces in the micrometer-range, Phys. Rev. Lett. 107, 171101 (2011), [arXiv:1108.2547 \[quant-ph\]](#)
- [6] **Jaco de Swart, Gianfranco Bertone, Jeroen van Dongen**, How Dark Matter came to matter, Nature Astronomy 1, 0059 (2017), [arXiv:1703.00013 \[astro-ph.CO\]](#)
- [7] **P. J. E. Peebles, Bharat Ratra**, The Cosmological Constant and Dark Energy (2002), [arXiv:astro-ph/0207347](#)
- [8] **Planck Collaboration**, Planck 2015 results. XIII. Cosmological parameters (2016), [arXiv:1502.01589 \[astro-ph.CO\]](#)
- [9] **N. Jarosik et al.**, Seven-Year Wilkinson Microwave Anisotropy Probe (WMAP) Observations: Sky Maps, Systematic Errors and Basic Results, Astrophys. J. Suppl. 192 14 (2011) [1001.4744], [arXiv:1001.4744 \[astro-ph.CO\]](#)
- [10] **M.C.Gonzalez-Garcia, Michele Maltoni**, Phenomenology with Massive Neutrinos, Phys.Rept.460:1-129,2008, [arXiv:0704.1800 \[hep-ph\]](#)
- [11] **Vernon Barger, Danny Marfatia, Kerry Lewis Whisnant**, The Physics of Neutrinos (2012), Princeton University Press, ISBN 0-691-12853-7
- [12] **Laurent Canetti, Marco Drewes, Mikhail Shaposhnikov**, Matter and Antimatter in the Universe, New J. Phys. 14 (2012) 095012, [arXiv:1204.4186 \[hep-ph\]](#)
- [13] **S. Weinberg**, Implications of Dynamical Symmetry Breaking, Phys. Rev. D13 (1976) 974–996, <https://doi.org/10.1103/PhysRevD.13.974>
- [14] **S. Weinberg**, Implications of Dynamical Symmetry Breaking: An Addendum, Phys. Rev. D19 (1979) 1277–1280, <https://doi.org/10.1103/PhysRevD.19.1277>
- [15] **L. Susskind**, Dynamics of spontaneous symmetry breaking in the Weinberg-Salam theory, Phys. Rev. D20 (1979) 2619–2625, <https://doi.org/10.1103/PhysRevD.20.2619>
- [16] **E. Gildener**, Gauge Symmetry Hierarchies, Phys. Rev. D14(1976) 1667, <https://doi.org/10.1103/PhysRevD.14.1667>

- [17] **Begeman, K. G., Broeils, A. H., Sanders, R. H.**, Extended rotation curves of spiral galaxies - Dark haloes and modified dynamics, Monthly Notices of the Royal Astronomical Society (ISSN 0035-8711), vol. 249, April 1, 1991, p. 523-537.
- [18] **Felix Kalhoefer**, Review of LHC Dark Matter searches, Int.J.Mod.Phys. A32 (2017) 1730006, [arXiv:1702.0243](#) [hep-ph]
- [19] **Philip Harris, Valentin V. Khoze, Michael Spannowsky, Ciaran Williams**, Closing up on Dark Sectors at Colliders: from 14 to 100 TeV, Phys. Rev. D 93, 054030 (2016), [arXiv:1509.02904](#) [hep-ph]
- [20] **Jing-Yuan, Edward W. Kolb, Lian-Tao Wang**, Dark matter coupling to electroweak gauge and Higgs bosons: an effective field theory approach, Phys.Dark Univ. 2 (2013) 200-218, [arXiv:1305.0021](#) [hep-ph]
- [21] **ATLAS Collaboration**, Search for dark matter produced in association with a Higgs boson decaying to two bottom quarks in pp collisions at $\sqrt{s} = 8$ TeV with the ATLAS detector, Phys. Rev. D 93, 072007 (2016), [arXiv:1510.06218](#) [hep-ex]
- [22] **ATLAS Collaboration**, Search for an invisibly decaying Higgs boson or dark matter candidates produced in association with a Z boson in pp collisions at $\sqrt{s} = 13$ TeV with the ATLAS detector, PLB 776 (2017), 318, [arXiv:1708.09624](#) [hep-ex]
- [23] **M. Cacciari, G.P. Salam and G. Soyez**, The anti- k_t jet clustering algorithm, JHEP 04 (2008) 063, [arXiv:0802.1189](#) [hep-ph]
- [24] **ATLAS collaboration**, Topological cell clustering in the ATLAS calorimeters and its performance in LHC Run 1, Eur. Phys. J. C 77 (2017) 490, [arXiv:1603.02934](#) [hep-ex]
- [25] **ATLAS collaboration**, Jet Calibration and Systematic Uncertainties for Jets Reconstructed in the ATLAS Detector at $\sqrt{s} = 13$ TeV, ATL-PHYS-PUB-2015-015 (2015) , <https://cdsweb.cern.ch/record/2028594>
- [26] **M. Cacciari, G.P. Salam and G. Soyez**, FastJet User Manual, Eur. Phys. J. C 72 (2012) 1896, [arXiv:1111.6097](#) [hep-ph]
- [27] **Tung-Mow Yan, Sidney D. Drell**, The Parton Model and its Applications, Int. J. Mod. Phys. A 29, 1430071 (2014), [arXiv:1409.0051](#) [hep-ph]
- [28] *Using $\gamma + jets$ to calibrate the Standard Model $Z(\rightarrow \nu\nu) + jets$ background to new processes at the LHC*
S. Ask, M. A. Parker, T. Sandoval, M. E. Shea, W. J. Stirling
 Cavendish Laboratory, University of Cambridge, CB3 0HE, UK; 2011
[\[arXiv:1107.2803\]](#)
- [29] *2017 Review of Particle Physics - Particle Listings*
C. Patrignani et al. (Particle Data Group)
 Chin. Phys. C, 40, 100001 (2016)
- [30] **J. Campbell, K. Ellis**, An update on vector boson pair production at hadron colliders, Phys. Rev. D 60 , 113006 (1999), [arXiv:hep-ph/9905386](#)
- [31] **J. M. Campbell, R. K. Ellis and C. Williams**, Vector boson pair production at the LHC, JHEP 1107, 018 (2011), [arXiv:1105.0020](#) [hep-ph]
- [32] **J. M. Campbell, R. K. Ellis and W. Giele**, A Multi-threaded Version of MCFM, EPJ C75, 246 (2015), [arXiv:1503.06182](#) [physics.comp-ph]
- [33] **John Campbell, Keith Ellis, Walter Giele, Ciaran Williams**, Monte Carlo for FeMtobarn processes (MCFM) v8.0 User Manual, <https://mcfm.fnal.gov/>

- [34] **R. K. Ellis, W. J. Stirling, and B. R. Webber**, QCD and Collider Physics, Cambridge Monographs, 2003
- [35] **J.M. Lindert, S. Pozzorini, et al.**, Precise predictions for V +jets dark matter backgrounds, Eur. Phys. J. C (2017) 77: 829, arXiv:1705.04664 [hep-ph]
- [36] **Sayipjamal Dulat, Tie Jiun Hou, Jun Gao, Marco Guzzi, Joey Huston, P. Nadolsky, Jon Pumplin, Carl Schmidt, Daniel Stump, C. P. Yuan**, New parton distribution functions from a global analysis of quantum chromodynamics, Phys. Rev. D 93, 033006 (2016), arXiv:1506.07443 [hep-ph]
- [37] **Jon Butterworth, Stefano Carrazza, et al**, PDF4LHC recommendations for LHC Run II, J. Phys. G: Nucl. Part. Phys. 43 023001 (2016), arXiv:1510.03865 [hep-ph]
- [38] **A.D. Martin, W.J. Stirling, R.S. Thorne, G. Watt**, Parton distributions for the LHC, Eur.Phys.J.C63:189-285,2009, arXiv:0901.0002 [hep-ph]
- [39] **A.D. Martin, W.J. Stirling, R.S. Thorne, G. Watt**, Uncertainties on α_s in global PDF analyses and implications for predicted hadronic cross sections, Eur.Phys.J.C64:653-680,2009, arXiv:0905.3531 [hep-ph]
- [40] **A.D. Martin, W.J. Stirling, R.S. Thorne, G. Watt**, Heavy-quark mass dependence in global PDF analyses and 3- and 4-flavor parton distributions, Eur.Phys.J.C70:51-72,2010, arXiv:1007.2624 [hep-ph]
- [41] **L. A. Harland-Lang, A. D. Martin, P. Motylinski, R. S. Thorne**, Parton distributions in the LHC era: MMHT 2014 PDFs, Eur. Phys. J. C (2015) 75: 204, arXiv:1412.3989 [hep-ph]
- [42] **The NNPDF collaboration, Ball, R.D., Bertone, V. et al.**, Parton distributions for the LHC Run II, J. High Energ. Phys. (2015) 2015: 40, arXiv:1410.8849 [hep-ph]
- [43] *LHAPDF6: parton density access in the LHC precision era*
Andy Buckley, James Ferrando, Stephen Lloyd, Karl Nordstrom, Ben Page, Martin Ruefenacht, Marek Schoenherr, Graeme Watt
arXiv:1412.7420
- [44] *Isolated photons in perturbative QCD*
S. Frixione
Phys. Lett.B429(1998)369–374, hep-ph/9801442